Synthesis and functionalization of biocompatible Tb:$CePO_4$ nanophosphors with spindle-like shape

Sonia Rodriguez-Liviano,[†] Francisco J. Aparicio,[†] Ana I. Becerro,[†] Jorge García-Sevillano,[‡] Eugenio Cantelar,[‡] Sara Rivera,[#] Yulán Hernández,[#] Jesus M. de la Fuente, [#] Manuel Ocaña[†]*

[†]Instituto de Ciencia de Materiales de Sevilla (CSIC-US), Americo Vespucio 49, Isla de La Cartuja, 41092 Sevilla, Spain.

[#]Instituto de Nanociencia de Aragon, Universidad de Zaragoza, Mariano Esquillor s/n, Zaragoza, 50018, Zaragoza, Spain

[‡] Dpto. Física de Materiales, C-04. Universidad Autónoma de Madrid, 28049 Madrid, Spain.

*Corresponding Author: Manuel Ocaña. E-mail: mjurado@icmse.csic.es

Abstract

Monoclinic Tb:$CePO_4$ nanophosphors with a spindle-like morphology and tailored size have been prepared though a very simple procedure, which consists of aging, at low temperature (120ºC), ethylene glycol solutions containing only cerium and terbium acetylacetonates and phosphoric acid, not requiring the addition of surfactants or capping agents. The influence of the heating mode (conventional convection oven or

microwave oven) and the Tb doping level on the luminescent, structural and morphological features of the precipitated nanoparticles have been also analyzed. This study showed that microwave-assisted heating resulted in an important beneficial effect on the luminescent properties of these nanophosphors. Finally, a procedure for the functionalization of the Tb:$CePO_4$ nanoparticles with aspartic-dextran is also reported. The functionalized nanospindles presented negligible toxicity for Verocells and a high colloidal stability when dispersed in water (pH=6.7), which along with theirs excellent luminescent properties, make them suitable for biomedical applications.

Key words: Nanoparticles · Cerium phosphate · Terbium · Luminescence · Functionalization· Aspartic-dextran

Introduction

Cerium(III) phosphate doped with Tb^{3+} cations ($Tb:CePO_4$) is a well known green emitting phosphor with low toxicity, high thermal and chemical stability, high luminescence efficiency and sharp emission bands, which finds important applications in chemical and biological sensing. For example, this phosphor has been recently proposed as an efficient oxygen sensor making use of the luminescence quenching produced when it is exposed to an oxidizing ambient, as a consequence of the partial oxidation of Ce^{3+} to Ce^{4+} (Di et al. 2010a). The application of this material for detection of molecules of biological interest, such as vitamin C, has been also suggested taking advantage of the recovering of luminescence occurred when previously oxidized $Tb:CePO_4$ nanophosphors are put into contact with such molecules (Di et al. 2010b). Finally, $Tb:CePO_4$ nanowires have been also used for bioimaging purposes (Zhang and Wong 2010).

For most of these uses, the control of particle morphology has been shown to be essential to optimize the nanophosphors performance (Chen et al. 2011). In particular, for biomedical applications, it has been well established that the particle geometry plays an important role in cell-material interactions, affecting cellular uptake and cell functioning. For example, Huang et al. (2010) have shown recently that anisometric nanoparticles are taken up by cells in larger amounts and have faster internalization rates than those with small aspect ratios. They also found that particles with larger aspect ratios have a greater impact on different aspects of cellular functions including cell proliferation, apoptosis, cytoskeleton formation, adhesion and migration. Particle size is another important issue for bioapplications. Thus, for biolabeling, especially for the sensitive analysis of molecules such as DNA, RNA or proteins, nanosized

phosphors are required, since their reduced size greatly increases surface area and, therefore, the biosensor sensitivity (Li et al. 2008). Therefore, the development of methods suitable for the fabrication of monoclinic Tb:$CePO_4$ nanophosphors with uniform morphologies and narrow size distribution in the nanometer range is of high interest.

Recently, several procedures for the synthesis of uniform Tb:$CePO_4$ based nanophophors with anysometric particle shape have been reported. Most of these methods conducted to long (in the micron range) nanowires (Bao et al. 2010, Bu et al. 2005, Di et al. 2010, Yu et al. 2009, Zhang et al. 2009, Zhang et al. 2010), nanorods (Komban et al. 2011) or nanotubes (Chen et al. 2008) with hexagonal structure. However, much fewer reports can be found regarding to $CePO_4$ nanoparticles with monoclinic structure, which is preferred since the presence of water in the hexagonal phase partially quenches the luminescence of this kind of phosphors (Niraj Luwang et al. 2011). Actually, to the best of our knowledge, only two precipitation methods have been developed which yield one-dimensional $CePO_4$ nanoparticles (<200 nm) with monoclinic structure, involving high synthesis temperatures (200ºC) and the use of toxic surfactants (CTAB) (Buchold and Feldman 2008) or complexing agents (EDTA) (Ma et al. 2008).

In this paper, we describe a much simpler (it does not require the use of toxic additives) low temperature (120ºC) route for the synthesis of Tb:$CePO_4$ nanophosphors with spindle-like morphology and narrow size distribution in the nanometer size range. The procedure is based on a homogeneous precipitation process in biocompatible ethylene glycol (EG) solutions containing only phosphoric acid (H_3PO_4) and Ln acethylacetonates ($Ln(acac)_3$) as phosphate and Ln precursors, respectively. We also have investigated the influence of the heating source (conventional convection oven or

microwave oven) on the morphological, structural and luminescent features of the precipitated nanoparticles, finding an important beneficial effect of microwave-assisted heating on the luminescent properties of these nanophosphors.

Finally, it is also well known that surface modification of the nanoparticles is important for most bioapplications since the surface properties determine the colloidal stability of the nanoparticles and the ability to provide anchors for adding functional ligands such as antibodies and drugs (Chatterjee et al. 2010). Although several biomedical applications have been suggested for Tb-$CePO_4$ nanophosphors, very few works dealing with their functionalization have been reported. In fact, we have only found in literature a recent work on the functionalization of Tb-$CePO_4$ nanorods with "Quat-primer" polymers (Komban et al. 2011). Herein, we also describe for the first time a procedure for the functionalization of the Tb-doped $CePO_4$ nanospindles with aspartic-dextran polymers. The so functionalized nanophosphors showed negligible toxicity and a high colloidal stability in aqueous dispersions, which make them suitable for biomedical applications.

Experimental section

Reagents

Cerium(III) acetylacetonate hydrate ($Ce(C_5H_7O_2)_3 \cdot xH_2O$, Aldrich, 99.9%), terbium acetylacetonate hydrate ($Tb(C_5H_7O_2)_3 \cdot xH_2O$, Aldrich, 99.9%), orthophosphoric acid (H_3PO_4, Aldrich, 85%) and ethylene glycol (EG, Fluka, < 99.5%) were used as received for the synthesis of nanoparticles. Albumin from bovine serum (BSA, ≥ 98% Sigma-Aldrich); tetraethylenepentamine (TEPA, $C_8H_{23}N_5$, Aldrich), sodium citrate tribasic

dehydrate ($C_6H_5Na_2O_7 \cdot 2H_2O$, ≥ 99.5 Sigma) and aspartic-dextran polymers were used for functionalization. Dextran from Leuconostoc mesenteroides (average mol wt 15,000-30,000, Sigma), sodium (meta)periodate (≥99.0%, Sigma-Aldrich), sodium borohydride (≥98,0% Sigma-Aldrich), L-aspartic acid (≥98%, Sigma), borane trimethylamine complex (>95%, Fluka), hydrochloric acid (37%, Prolabo), sodium hydroxide (≥98%, Sigma-Aldrich) and sodium acetate anhydrous (>99.5%, Fluka) were used for the synthesis of aspartic-dextran.

Synthesis of nanospindles

Weighted amounts of $Ce(acac)_3$ and $Tb(acac)_3$ were dissolved in EG under magnetic stirring while heating at low temperature (~75ºC) to favor dissolution. Then, these solutions were cooled to room temperature and proper amounts of phosphoric acid were admixed so that the final H_3PO_4 concentration was 0.15 mol dm^{-3}. The final Ce+Tb concentration was kept constant at 0.004 mol dm^{-3}, whereas the Tb/Ce+Tb ratio was varied in the 0-15% molar range. After homogenization, the final solutions (total volume = 10 cm^3) placed in tightly closed reactors were aged at 120ºC in a convection oven preheated at such temperature (hereafter it will be referred as conventional heating, CH) or in a microwave oven (Sineo MDS-8), which was heated at the target temperature using a heating rate of 14ºC min^{-1} (hereafter it will be referred as MW heating). The dispersions obtained after aging were cooled down to room temperature, centrifuged to remove the supernatants and washed twice with ethanol and once with double distilled water. Finally, the precipitates were dispersed in water. For some specific analyses, the powders were dried at room temperature.

For functionalization, solutions with adjusted pH of sodium citrate (20 mmol dm^{-3}, pH=4-13), BSA (10 μg cm^{-3}, pH=5), TEPA (20 mmol dm^{-3}, pH=5-8) and aspartic-dextran (20% oxidized) (0.18 mmol dm^{-3}, pH=5-8) were first prepared. Then, a weighted amount of Tb:$CePO_4$ nanoparticles was added to such solutions so that their final concentration was 0.06 mg cm^{-3}. The resulting dispersions were sonicated in cold water during 1 h. After this treatment, the so functionalized nanoparticles were washed several times with MilliQ water by centrifugation and finally redispersed in MilliQ water. The aspartic-dextran polymers solutions were prepared following a procedure previously reported by Fuentes et al. (2004) (details are provided in supporting information).

Characterization

Particle shape was examined by transmission (TEM, Philips 200CM) electron microscopy. Particle size distributions were obtained by counting several hundreds of particles from the TEM micrographs.

EDX spectroscopy couplet to the TEM microscope was used to obtain information on the particles composition. The quantitative composition of the samples was analyzed by inductively coupled plasma atomic emission spectroscopy (ICP-AES, Horiba Jobin Yvon, Ultima 2).

The crystalline structure of the prepared samples was assessed by X-ray diffraction (XRD, Panalytical, X´Pert Pro with an X-Celerator detector). Unit cell parameters were determined from the XRD data (collected at intervals of 0.03° (2θ) for an accumulation time for interval of 3000 s) by using the Rietveld method with the JANAsoftware (Petricek et al. 2006). The starting parameters were taken from (Ni et al. 1995). To gain

additional information on the structural features of the synthesized nanoparticles, they were also characterized by high resolution transmission electron microscopy (HRTEM, Philips 200CM). The digital diffraction patterns (DDP) were obtained from the HRTEM images using Digital Micrograph software.

The infrared spectra (FTIR) of the nanophosphors diluted in KBr pellets were recorded in a Jasco FT/IR-6200 Fourier transform spectrometer. Thermogravimetric analyses (TGA) were performed in air at a heating rate of 10°C min^{-1}, using a Q600 TA Instrument.

The excitation and emission spectra of the nanophosphors dispersed in water (0.5 mg cm^{-3}) were recorded in a Horiba Jobin-Yvon Fluorolog3 spectrofluorometer operating in the front face mode. Lifetime measurements have been performed under pulsed excitation (10 ns) by using a Nd:YAG laser (Spectra Physics model DCR 2/2A 3378) linked to a harmonic generator. The fourth harmonics at 266 nm has been selected for Ce^{3+} excitation. Tb^{3+} luminescence at λ = 544 nm ($^5D_4 \rightarrow {}^7F_5$ transition) was detected by using a photomultiplier tube and averaged by a digital oscilloscope. The photographs showing the luminescence of the nanophosphors in water dispersions were taken under illumination with ultraviolet radiation (λ= 254 nm), filtered from a Hg discharge a lamp.

The X-ray photoelectron spectra (XPS) of the samples were measured with a VG Escalab apparatus (Model 220) using the AlKα excitation source. Calibration of the spectra was done at the P2p peak corresponding to phosphate group taken at 132.4 eV (Wagner et al. 1973).

Z potential measurements were carried out in a Malvern Zetasizer Nano-ZS90 apparatus. The isoelectric point (i.e.p.) of the nanophosphors was determined by measuring the values of Z potential as a function of pH. For this, the nanophosphors were dispersed in 0.01 mol dm^{-3} NaCl solutions to keep the ionic strength constant, and

the pH was varied by adding HCl or NaOH as needed. After adjusting pH, the suspensions were stabilized overnight.

The colloidal stability of the nanophosphors suspensions having a nanoparticle content of 0.5 mg cm^{-3} was monitored by analyzing the evolution of their UV-visible absorbance spectrum with aging time.

Cell culture

Vero (monkey kidney epithelial cells) were cultured in Dulbecco's Modified Eagle's Medium (DMEM), supplemented with 10% fetal bovine serum (FBS), 5% glutamine and 5% penicillin/streptomycin. Cell cultures were incubated at 37ºC and equilibrated in 4% CO_2 and air.

Viability Testing

Cell viability and proliferation were analyzed by the MTT colorimetric assay. For the cytotoxicity assay 5000 cells were seeded in each well of 96-well plates and grown for 24 h. After 24 h, the medium was replaced with fresh medium containing the different types of nanoparticles in varying concentrations. After cultivation again for 24 h, 20 µL of MTT dye solution (5 mg/mL in PBS) was added to each well. After 4 h of incubation at 37 °C and 5% CO_2, the medium was removed, the cells were washed with fresh medium, and formazan crystals were dissolved in 100 µL of DMSO. The absorbance of each well was read on a microplate reader (Biotek ELX800) at 570 nm. The spectrophotometer was calibrated to zero absorbance using culture medium without cells. The relative cell viability (%) related to control wells containing cell culture

medium without nanoparticles was calculated by [A]test/[A]control x100. Each measurement was repeated at least five times to obtain the mean values and the standard deviation.

Results and discussion

Synthesis and characterization of nanophosphors

It has been well documented that to obtain uniform particles by precipitation, a homogeneous process is required, which can be achieved through a slow and controlled release of the precipitating anions or cations in the reaction medium (Matijević 1993). In this work, we have employed the latter strategy using $Ln(acac)_3$ (Ln = Ce and Tb) as precursors. These compounds can be decomposed in solution on heating, thus liberating the Ln^{3+} cations in a controlled manner (Nuñez and Ocaña 2007)**,** which may react with phosphate anions forming the desired Tb:$CePO_4$ particles. EG was selected as solvent because such Ln precursors are not water soluble and mainly, because polyols have been amply shown to be suitable solvents for the synthesis of nanomaterials, since they may act not only as solvent but also as capping agent, thus limiting particle growth (Poul et al. 2003, Feldmann, 2003).

As observed in Fig. 1a, the conventional heating at 120ºC for 1 h of 0.004 mol dm^{-3} $Ce(acac)_3$ solutions in the presence of 0.15 mol dm^{-3} H_3PO_4 gave rise to rather uniform nanoparticles with spindle-like shape having a length of 244±40 nm and a width of 57±11 nm (axial ratio = 4.3) (Table 1). According to XRD (Fig. 2), these nanospindles consisted of monoclinic $CePO_4$ (JCPDS No 32-199). The crystal size (see Table S1 in supplementary information) estimated by using the Scherrer formula from several XRD

peaks (200, -122 and -202) was much smaller (in the 10-20 nm range) than the spindles dimensions indicating that they were polycrystalline. This observation also seems to indicate that they were formed through an aggregation process of smaller subunits, which is also suggested by the observation of the precipitates as increasing aging time (see Fig. S2 in supplementary information). Thus, after 7 min, a mixture of some spindles were already formed, although a certain amount of much smaller elongated particles were also present, which were consumed on prolonged aging up to 15 min.

The $CePO_4$ particles obtained by using the MW heating mode, keeping constant the other synthesis parameters (reagent concentration, temperature, aging time) also had spindle-like shape (Fig. 1b), although they were smaller (171±47 x 48±8 nm) and presented a lower axial ratio (3.6) than those obtained by conventional heating (Table 1), in spite of the higher reaction yield associated to the former method (78%) when compared with the latter (71%). The change in the heating mode also has significant effects on the structural characteristics of the nanospindles. Thus, although the MW-assisted synthesis also resulted in the monoclinic phase (Fig. 2), the crystal sizes calculated from the different reflections for this sample were much higher than those estimated for the sample obtained by conventional heating. In particular, the crystal size corresponding to the 200 reflection ($2\theta \sim 27^{o}$) was similar (40 nm) to the shorter spindle dimension (48 nm), whereas the values corresponding to the -122 ($2\theta \sim 31.2^{o}$) and -202 ($2\theta \sim 34.5^{o}$) reflections were closer (100-96 nm) to the spindle longest dimension (171 nm). This finding suggests that the nanoparticles obtained in the microwave oven were single crystals in contrast with the polycrystalline character of those obtained by conventional heating. The observation of Fig. 2 also indicates that the intensity of the 120 reflection corresponding to the sample prepared by MW heating is clearly much higher than that of the JCPDS file. This preferential orientation seems to indicate that

the spindles grow along the crystallographic *c* axis. The HRTEM images (Fig. 1c) and the DDP pattern obtained for this sample (Fig. 1c, inset) gave a further support to such suggestions. Thus, the DDP image obtained from the HRTEM micrograph showed several spots, which could be associated to the (-120), (-111) and (011) crystallographic planes of the monoclinic $CePO_4$ phase (JCPDS No 32-199), confirming the monocrystalline character of the spindle. In addition, two sets of planes with an interplanar distance of 4.6 and 3.09 Å, respectively, were clearly observed in the HRTEM image, which correspond to the (001) and (120) planes of the monoclinic structure, the latter being parallel to the longest dimension of the spindle. Therefore, such observation is in agreement with their preferential growth along the crystallographic *c* axis. The monocrystalline character of these nanoparticles indicates a growth mechanism different from that associated to the conventional heating. In fact, in contrast with the latter case, it was found that after 7 min (time required to reach 120ºC at the selected heating rate), the final spindles were already formed, with a size similar to the final value indicating that nanoparticles formation was faster.

To explain these different formation mechanisms, it must be taken into account that the heat transmission in the CH system is slow and takes place from the reactor wall to the inner creating a temperature gradient, which gives a chance for secondary nucleation events and for the aggregation of nuclei during their growth. However, under MW irradiation, EG with the OH groups absorbs vast amounts of microwave energy increasing the temperature of the system rapidly and also the diffusion rate (Zhu et al 2010). Consequently, a faster nucleation rate is expected in this case, reducing the probability of heterogeneous nucleation. In addition, it must be noticed that in the WW assisted heating mode, a dielectric heating of the positive and negative ions and polar molecules of solvent (Lewis et al. 1992) takes place, which is originated from the

dissipation of energy into heat as an outcome of agitation and intermolecular friction of molecules when dipoles change their mutual orientation at each alternation of the electric field at a very high frequency (Nyutu et al. 2008). It has been argued (Zhu et al. 2010) that as a consequence of such dielectric heating, after the nucleation stage, most of the precipitating ions are distributed around nuclei well-proportioned, which facilitate the growth of each orientation yielding well crystallized particles.

Finally, in order to explain the spindle-like morphology and the preferential growth along the *c* axis of monoclinic $CePO_4$ we must take into account that 1D nanostructures can be formed in solution by employing solid or surfactants templates (not used here), by the addition of capping agents which are adsorbed preferentially on certain crystal faces, or favored by an anisotropic crystal structure (Xia et al. 2003, Zhang et al. 2003). In our case, although EG could act as capping agent, this possibility must be disregarded on the basis of the FTIR spectrum of the precipitated particles (Fig. 3), which only showed several bands at <1250 cm^{-1}, which are characteristics of the $CePO_4$ lattice (Ma et al. 2008), along with two additional absorptions at ~3400 and 1630 cm^{-1} due to a hydroxyl anions and/or water (Nakamoto 1986). Therefore, it can be considered that as previously suggested for other one-dimensional $CePO_4$ nanostructures (Ma et al. 2008), the main driving force for the formation of nanospindles is the highly anisotropic monoclinic $CePO_4$ structure, which involves ninecoordinated lanthanide atoms apically combined by the distorted tetrahedral phosphate groups forming chains (Mullica et al. 1984).

By using the conventional heating mode, the $CePO_4$ spindles could be doped with increasing amounts of Tb^{3+} cations (in the 2-15% molar range) keeping a rather good uniformity (see Fig. S3 in supplementary information), although a progressive increase of the length (from to 244 to 821 nm) and a decrease of the axial ratio (from 4.3 to 2)

(Table 1) could be detected. The Tb/Ce+Tb mol ratio measured by ICP-AES for the doped samples was very similar to the nominal value (see Table S2 in the supplementary information) suggesting the success of the doping procedure. The incorporation of the Tb^{3+} cations to the $CePO_4$ spindles was confirmed by the EDX spectra recorded for single particles (Fig. S4 in supplementary information), which showed the presence of the Tb peaks in addition to those of O, Ce and P. All doped samples also presented the monoclinic structure as indicated by XRD (see Fig. S5 in supplementary information). Moreover, the crystal size obtained from broadening of the XRD reflections (see Table S1 in supplementary information) was found to progressively increase at increasing the Tb content, although the estimated values were still lower than the particles dimensions indicating that they were polycrystalline as the undoped $CePO_4$ sample. It was also found that the position of the XRD reflections shifted to higher values of 2θ suggesting the formation of Tb-$CePO_4$ solid solutions, which was confirmed by the measurements of the unit cell parameters of the doped samples (Table 2). Thus, a linear decrease of the unit cell volume was detected as increasing the Tb doping level (Fig. 4) in agreement with the smaller size of the Tb^{3+} cations (1.04 Å) when compared to that of Ce^{3+} (1.14 Å) (Shanon 1976).

Microwave heating also yielded uniform Tb-doped $CePO_4$ spindles (see Fig. S6 in supplementary information) if the nominal amount of Tb^{3+} was kept ≤ 2%, although their mean size slightly increased (216 x 58 nm) with respect to the undoped system (Table 1). At higher Tb contents (in the 5-15% range), certain heterogeneity in particle size and shape was detected (see Fig. S6 in supplementary information), for which, these samples were discarded for further characterizations. XRD (see Fig. S7 in supplementary information) revealed that the $Tb_{0.02}Ce_{0.98}PO_4$ nanospindles also crystallized with the monoclinic structure and that, according to the broadening of the

XRD reflections (similar to that of the undoped sample), they were single crystals. The agreement observed between the nominal and experimental Tb contents for this uniform nanophosphor (see Table S2 in the supplementary information) and the unit cell contraction detected when compared with the undoped nanospindles (Table 2), clearly evidenced the success of the incorporation of the Tb^{3+} cations to the $CePO_4$ lattice. It is noticeable that the unit cell parameters measured for this sample prepared by MW heating were lower than the values obtained for the samples synthesized by conventional heating with the same Tb content (Table 2), which might be associated to the lower crystal size of the latter. In fact, unit cell expansions have been previously observed as decreasing crystal size for many oxide materials and attributed to several factors related to the presence of structural disorder (dislocations, vacancies, impurities, confinement effects) in very small crystals (Gamarnik 1992, Zang et al. 2002, Imteyaz Amaz et al. 2009, Lemine et al. 2010).

Luminescent properties.

It is well known that the green luminescence of $Tb^{3+}$is usually weak since the electronic transitions within the $4f^n$ configuration of Tb^{3+} are strongly forbidden, and that, in the presence of Ce^{3+} cations, the intensity of such luminescence is greatly increased through an energy transfer process from Ce^{3+} to Tb^{3+} (Blasse and Brill 1967). In order to analyze the emission properties of our Tb-doped nanoparticles, we evaluated first that of the undoped ones for comparison.

The excitation and emission spectra of the undoped $CePO_4$ spindles synthesized by conventional heating are shown in Fig. 5. In agreement with previous reports, the excitation spectrum (monitored at 352 nm) consisted of a broad band at 273 nm and a

shoulder at 255 nm, which are due to 4f→5d electronic transitions of Ce^{3+} (Riwotzki et al. 2000). Also as expected, the emission spectrum, which was recorded using an excitation wavelength of 255 nm for a better observation of all the emission features of the Ce^{3+} ions, displayed a broad band centred at 352 nm corresponding to the transition from the excited $5d^1$ configuration to the $^2F_{5/2}$ and $^2F_{7/2}$ levels of Ce^{3+} (Guan et al. 2007). As observed in Fig. 6 (top), the excitation spectrum monitored at the main Tb emission line at 542 nm (Riwotzki et al. 2000) for sample $Tb_{0.02}Ce_{0.98}PO_4$ prepared by conventional heating was quite similar to that of undoped $CePO_4$ (Fig. 5) indicating that the Tb emission is produced after an energy transfer from excited Ce^{3+} to Tb^{3+} cations, which confirmed the success of the doping procedure. The emission spectra obtained for all Tb doped samples prepared by conventional heating (Fig. 6, bottom) clearly showed the characteristics emissions of Tb^{3+} (from 450 to 650 nm) arising from the $^5D_4$-^7F_j (J = 6, 5, 4, 3) transitions (Guan 2007), the most intense appearing at 542 nm, which is the main responsible for the green luminescence of this nanophosphor (inset in Fig. 6, bottom). The broad band associated to the Ce ions was still detected in these spectra, which indicated that the energy transfer from the latter to the Tb cations was not complete. Fig. 6 (bottom) also shows that the increase of the Tb content from 2 to 15% resulted in an increase of the emissions intensity, in apparent contrast with a previous report on Tb:$CePO_4$ nanowires, which has showed a decrease of luminescence intensity above a 5% Tb content due to the well known concentration quenching effect (Bao et al. 2010). In order to get information on the luminescence efficiency of our samples, the values of lifetime for the $^5D_4$ Tb^{3+} manifold were measured after pulsed excitation using the fourth harmonics of a Nd:YAG laser (λ_{exc} = 266 nm). It was verified that the emission spectra under this excitation are coincident with those obtained after 255 nm excitation shown in Fig. 6. The normalized temporal decays of the $^5D_4$ level, measured

at λ_{em} = 544 nm ($^5D_4 \rightarrow {}^7F_5$ transition), for different Tb concentrations are shown in Fig. 7. The observed Tb luminescence decays are multi-exponential, as it has been reported for other nano-crystalline hosts (K. Riwotzky 2000, Pankratov 2010). In order to quantify the decay we have used the effective lifetime, τ, which is defined as (Inokuti 1965):

$$\tau = \int_0^\infty t\, I(t)\, dt \Big/ \int_0^\infty I(t)\, dt$$

It can be observed that the emission lifetime varies from τ = 1.05 ms to τ = 0.54 ms when terbium concentration is increased from 2% to 15%, as it is depicted in the inset of Fig. 7. It has been also checked that the same values are obtained when the decays are measured in the other luminescence bands associated to the radiative decay from the $^5D_4$ Tb level. Consequently, it can be concluded that concentration quenching is also present in our samples for doping levels above 2%, in agreement with previous reports (Bao et al 2010). The increase of luminescence observed as increasing the Tb content must be then mainly attributed to the increase of luminescence centers, although the increase of crystallite size as increasing the Tb content (see Table S1 in the supplementary information), should also have a positive effect on the increase of the Tb luminescence since crystal imperfections may act as effective luminescence quenchers (Zhu 2010).

As expected, the features of the excitation and emission spectra of the $Tb_{0.02}Ce_{0.98}PO_4$ nanophosphor prepared by MW-assisted heating (Fig. 8) were found to be similar to those of the samples prepared by conventional heating. However, as observed in Fig. 8 (bottom), the intensity of the emissions of the former (Tb doping level = 2%) was even higher than that associated to the sample prepared by conventional heating having the strongest emission ($Tb_{0.15}Ce_{0.85}PO_4$), which contained a much higher Tb content (15%). This finding is in agreement with lifetime measurements (Fig. 7) since the lifetime

value obtained for the sample synthesized by MW heating was much (τ = 1.86 ms) higher than those corresponding to all samples prepared by conventional heating (Fig. 7, inset), which ranged from 0.54 (15% Tb) to 1.04 ms (2%Tb). To explain the higher luminescence efficiency in the sample prepared by MW-assisted heating, we must take into account that crystal imperfections and the presence of impurities are among the main known factors that may quench the luminescence of lanthanide ions. An additional cause of luminescence quenching in Tb^{3+}/Ce^{3+} codoped systems is the partial oxidation of Ce^{3+} to Ce^{4+} (Di et al, 2010a). In our case, the only impurity contained in the nanospindles prepared according to the two heating methods was a certain amount of hydroxyl anions and/or water molecules (see Fig. S8 in supplementary information), as also observed for the undoped samples (Fig. 3). TGA analyses (Fig. S9 in supplementary information) revealed that the amount of these impurities contained in both kinds of samples was very similar (~6%), which suggest that the quenching by impurities does not seem to be the main cause of their different luminescence intensity. In order to identify the Ce oxidation state in these samples, their XPS spectra were also recorded. As observed in Fig. 9, almost identical spectroscopic features were detected for the two main Ce3d peaks measured for both samples, which appeared at the binding energy (903.5 and 885.3 eV) expected for Ce^{3+} species (Di et al. 2010a). The presence of Ce^{4+} in both samples can be disregarded in view of the absence of a peak at a binding energy of 917 eV, which is characteristic of tetravalent cerium (Di et al. 2010a). Therefore, we conclude that the much stronger luminescence of the sample prepared by microwave-assisted heating is due to its much higher crystallinity, as detected by XRD and HRTEM measurements.

It should be noted that the lifetime obtained for our optimum nanophosphor ($Tb_{0.02}Ce_{0.98}PO_4$ synthesized by MW-assisted heating) (τ = 1.86 ms) was among the

highest values so far reported for this system (1.4-1.97 ms) (Yu et al 2009, Li et al 2010). This sample was then selected for functionalization, colloidal stability measurements, and citotoxicity analyses.

Functionalization and cell viability

For the functionalization of the nanophosphors different charged molecules were used at different pH to be linked to the nanoparticles by ionic adsorption, such as BSA, citrate, TEPA or aspartic-dextran polysaccharide synthesized as described in Supporting Information. Among them, the only successful functionalization methodology was that using aspartic-dextran polysaccharide working at pH = 5, which was substantiated by FTIR spectroscopy. Thus, the spectrum of the functionalized nanoparticles (Fig. 11) displayed bands in the 1400-1600 cm^{-1} region, similar to those of aspartic-dextran polymer indicating the presence of these species on the nanoparticles surface. It should be noted that at pH = 5, aspartic-dextran is negatively charged, while the surface of the nanoparticles, whose i.e.p. was 6.7 (Fig. 10), is positively charged, guaranteeing ionic interactions between nanoparticles and polymer. The establishment of multipunctual interactions between the carboxilated dextran and the nanoparticles reinforce the ionic interactions making the dextran-nanoparticles more stable.

The success of the functionalization procedure was further confirmed by the surface charge reversal observed for the functionalized nanoparticles (Z potential = -19 mV, at pH = 5.1) when compared with the untreated ones (Z potential = 7.3 mV, at pH =5.1). The amount of aspartic-dextran species attached to the nanoparticles surface was quantified by TGA analysis. As observed in Fig. 12, the TGA curve obtained before functionalization showed a weight loss of 4% in the 25-230ºC range mainly due to the

release of water, whereas that of the functionalized sample presented and additional weight loss of 4.5% in the 230-800ºC range associated to the decomposition of the adsorbed organic species. It is important to mention that the Tb luminescence intensity remained almost unaltered after functionalization (Fig. S10 in supplementary information) indicating the absence of significant quenching associated to the adsorbed aspartic-dextran ploymer.

The UV-visible absorbance spectra recorded for suspensions in water (pH=6.7) of the Tb:$CePO_4$ nanophosphor after different aging times up to 24 h (Fig. 13) showed the expected two bands at 260 and 275 nm due to the absorption of phosphate groups (Zhang et al. 2010). The lack of variation of the intensity of these bands on aging discarded the presence of sedimentation thus manifesting the high colloidal stability of such suspenions in aqueous media.

Biocompatibility studies of the nanophosphors were undertaken by evaluating the cell viability of Vero cells by the MTT assay [Mosmann 1993]. This assay relies on the mitochondrial activity of fibroblasts activity of fibroblasts and represents a parameter for their metabolic activity. The MTT (3-(4,5-dimethylthiazol-2-yl)-2,5-diphenyltetra-zolium bromide) assay is a simple non-radioactive colorimetric assay to measure cell cytotoxicity, proliferation, or viability. MTT is a yellow, water-soluble tetrazolium salt. Metabolically active cells are able to convert this dye into a water-insoluble dark-blue formazan by reductive cleavage of the tetrazolium ring. Formazan crystals, then, can be dissolved in an organic solvent such as dimethylsulphoxide (DMSO) and quantified by measuring the absorbance of the solution at 550 nm, and the resultant value is related to the number of living cells. The metabolic activity and proliferation of fibroblasts was thus measured after 24 hours' culture, and showed negligible toxicity effects (Fig. 14) with viability percentages as high as 80-90% for concentrations up to 0,5 mg/mL.

Conclusions

We have shown that the aging of ethylene glycol solutions containing cerium and terbium acetylacetonates and phosphoric acid at low temperature (120ºC) in a conventional oven yields, under proper reagents concentrations, polycrystalline Tb:$CePO_4$ nanophosphors with a spindle-like morphology and monoclinic structure. The size of these nanoparticles was found to increase as the Tb content increased, whereas their axial ratio decreased. We have also demonstrated that the use of microwave assisted heating instead of the conventional heating mode resulted in smaller nanospindles with much higher crystallinity (single crystals), which has an important beneficial effect on the on the luminescent properties of these nanophosphors, which could be further functionalized with aspartic-dextran polymers providing anchors for adding functional ligands such as antibodies and drugs. These features along with the negligible toxicity of these functionalized nanophosphors and their stability when dispersed in aqueous media make them suitable for biomedical applications.

Acknowledgements. This work has been supported by Junta de Andalucía (grant FQM6090), the Spanish CICYT (Grant MAT2011-23593) and ERC-Sarting Grant NANOPUZZLE. S. R. Liviano wants to thank the Spanish Ministerio de Ciencia y Tecnología for an FPI fellowship. J.M.F. wants to thank ARAID for financial support. Authors thank V. Grazu for fruitful discussion and I. Echaniz for technical support.

References

Bao J, Yu R, Zhang J, Wang D, Deng J, Chen J, Xing X (2010) Scripta Mater 62:133-136

Blasse G, Brill A (1967) J Chem Phys 47:1920-1926

Bu W, Hua Z, Chen H, Shi J (2005) J Phys Chem B 109:14461-14464

Buchold BHM, Feldman C (2008) Adv Funct Mater 18:1002-1011

Chatterjee DK, Gnanasammandhan MK, Zhang Y (2010) Small 6:2781-2795

Chen G, Sun S, Zhao W, Xu S, You T (2008) J Phys Chem C 112:20217-20221

Chen Y, Chen H, Zhang S, Chen F, Zhang L, Zhang J, Zhu M, Wu H, Guo L, Feng J, Shi J (2011) Adv Funct Mater 21:270-278

Di W, Wang X, Ren X (2010) Nanotech 21:075709 (a)

Di W, Shirahata N, Zheng A, Sakka Y (2010) Nanotech 21:365501 (b)

Feldmann C (2003) Adv Funct Mater 13:101-107

Fuentes M, Mateo C, García L, Tercero JC, Guisán JM, Fernández-Lafuente R, (2004) Biomacromolecules 5:883-888

Gamarnik MY (1992) phys stat sol 170:27-37

Guan M, Sun, J, Han M, Xu Z, Tao F, Yin G, Wei X, Zhu J, Jiang X (2007) Nanotech 18:415602

Huang XL, Teng X, Chen D, Tang FQ (2010) Biomaterials 31:438-448

Imteyaz Ahmad MD, Bhattacharya SS (2009) Appl Phys Letters 95:191906

Inokuti M, Hirayama F (1965) J Chem Phys 43, 1978-1989

Komban R, Beckmann R, Rode S, Ichilmann S, Kühnle, Beginn W, Haase M (2011) Langmuir 27:10174-10183

Lemine OM, Sajieddine M, Bououdina M, Msalam R, Mufti S, Alyamani A (2010) J Alloys Comp 502:279-282

Lewis DA, Summers JD, Ward TC, McGrath JEJ (1992) J Polym Sci 30A:1647-1653

Li H, Zhu G, Ren H, Li Y, Hewitt IJ, Qiu S (2008) Eur J Inorg Chem 2033-2037

Li Y, Sun Z, Lun M, Zhang X, Yao M, Joly AG, Liu Z, Chen W (2010) Nanotech. 21:125604 (7 pp)

Ma L, Che WX, Zheng YF, Xu ZD (2008) Mater Res Bull 43:2840-2849

Matijević E (1993) Chem Mater 5:412-426

Mosmann, TJ (1993) J Immunol Methods 95:55-63

Mullica DF, Milligan WO, Grossie DA, Beall GW, Boatner LA (1984) 95:231-236

Nakamoto K (1986) Infrared and Raman Spectra of Inorganic and Coordination Compounds, John Wiley & Sons, New York.

Ni YX, Hughes JM, Mariano AN (1995) Amer Miner 80:21-26

Niraj Luwang M, Ningthoujam Jagannath RS, Srivastava SK, Vatsa RK (2010) J Am Chem Soc 132:2759-2768

Nuñez NO, Ocaña M (2007) Nanotech 18:455606

Nyutu EK, Chen CH, Dutta PK, Suib SL (2008) J Phys Chem C 112:9659-9667

Pankratov V, Popov AI, Chernov SA, Zharkouskaya A, Feldmann C (2010) Phys Status Solidi B 247:2252-2257

Petricek V, Dusek M, Palatinus L (2006) Institute of Physics, Academy of Sciences of the Czech Republic, Praha. http://www-xray.fzu.cz/jana/jana.html

Poul L, Ammar S, Jouini N, Fievet F (2003) J Sol-Gel Sci Tech 26:261-265

Riwotzki K, Meyssamy H, Kornowski A, Haase M (2000) J Phys Chem B 104:2824-2828

Shannon RD (1976) Acta Cryst A32:751-767

Wagner D, Riggs WH, Davis LE, Moulder JF, Muilinberg GE (1973) Handbook of X-Ray Photoelectron Spectroscopy, Perkin-Elmer Corporation, Minnesota

Xia Y, Yang P, Sun Y, Wu Y, Mayers B, Gates B, Yin Y, Kim F, Yan H (2003) Adv Mater 15:353-389

Yu C, Yu M, Li C, Liu X, Yang J, Yang P, Lin J (2009) J Solid State Chem 182:339-347

Zhang F, Chan SW, Spanier JE, Apak E, Jin Q, Robinson RD, Herman IP (2002) Appl Phys Letters 80:127129

Zhang YW, Yang ZG, You LP, Si R, Yan CH (2003) Eur J Inorg Chem 4099-4104

Zhang C, Chen J, Zhu X, Zhou Y, Li D (2009) Chem Mater 21:3570-3575

Zhang F, Wong SS (2010) ACS Nano 4:99-112

Zhu X, Zhang Q, Li Y, Wang H (2010) J Mater Chem 20:1766-1771

Table 1: Size and axial ratio of the Tb:$CePO_4$ particles synthesized by using conventional or microwave heating.

Sample	Tb/Tb+Ce (% molar)	Heating mode	Length (nm)	Width (nm)	Axial ratio L/W
$CePO_4$	0	Conventional	244±40	57±11	4.3
$Tb_{0.02}Ce_{0.98}PO_4$	2	Conventional	318±48	81±16	3.9
$Tb_{0.05}Ce_{0.95}PO_4$	5	Conventional	409±70	128±21	3.2
$Tb_{0.10}Ce_{0.90}PO_4$	10	Conventional	650±108	277±60	2.4
$Tb_{0.15}Ce_{0.85}PO_4$	15	Conventional	821±95	410±47	2.0
$CePO_4$	0	Microwave	171±47	48±8	3.6
$Tb_{0.02}Ce_{0.98}PO_4$	2	Microwave	216±42	58±8	3.7
$Tb_{0.05}Ce_{0.95}PO_4$	5	Microwave	256±70	74±13	3.4
$Tb_{0.10}Ce_{0.90}PO_4$	10	Microwave	170±62	68±18	2.5
$Tb_{0.15}Ce_{0.85}PO_4$	15	Microwave	103±29	41±10	2.7

Table 2. Unit cell parameters of the monoclinic Tb:$CePO_4$ samples synthesized by using conventional or microwave heating. Errors are included in parenthesis.

Sample	Tb/Tb+Ce (% molar)	Heating mode	a (Å)	b (Å)	c (Å)	β (º)
$CePO_4$	0	Conventional	6.8143(34)	7.0303(30)	6.4807(30)	103.897(40)
$Tb_{0.02}Ce_{0.98}PO_4$	2	Conventional	6.8107(25)	7.0326(24)	6.4835(23)	103.973(28)
$Tb_{0.05}Ce_{0.95}PO_4$	5	Conventional	6.8001(24)	7.0203(23)	6.4800(22)	103.995 (25)
$Tb_{0.10}Ce_{0.90}PO_4$	10	Conventional	6.7884(24)	7.0007(21)	6.4738(21)	104.011(23)
$Tb_{0.15}Ce_{0.85}PO_4$	15	Conventional	6.7799(26)	6.9967(23)	6.4634(23)	104.046(27)
$CePO_4$	0	Microwave	6.7960(9)	7.0184(8)	6.4707(8)	103.817(9)
$Tb_{0.02}Ce_{0.98}PO_4$	2	Microwave	6.7887(5)	7.0090(4)	6.4653 (4)	103.840(5)

Figures

Fig. 1. TEM images of the $CePO_4$ nanoparticles prepared by aging at 120ºC for 1 h 0.004 $Ce(acac)_3$ mol dm^{-3} and 0.15 mol dm^{-3} H_3PO_4 solutions in EG using a conventional (a) or microwave oven (b). HRTEM image and DDP pattern obtained for a single $CePO_4$ nanospindle synthesised by using microwave heating (c).

Fig. 2. X-ray diffraction patterns recorded for the samples shown in Fig. 1. The JCPDS file for monoclinic $CePO_4$ is also included.

Fig. 3. FTIR spectra recorded for the samples shown in Fig. 1

Fig. 4. Unit cell volume obtained for the Tb:$CePO_4$ samples synthesised by using conventional heating with different Tb content

Fig. 5. Excitation (λ_{em}= 352 nm) and emission (λ_{ex}= 255 nm) spectra of the undoped $CePO_4$ spindles synthesized by using conventional heating

Fig. 6. Excitation spectrum (λ_{em}= 542 nm) of the $Tb_{0.02}Ce_{0.98}PO_4$ sample obtained by using conventional heating (top) and emission spectra (λ_{ex}= 255 nm) of the Tb:$CePO_4$ samples synthesized by conventional heating with different Tb content (bottom). Inset: photograph showing the green luminescence of aqueous suspension of the $Tb_{0.15}Ce_{0.85}PO_4$ phosphor under UV illumination.

Fig. 7. Decay curves obtained after excitation at 266 nm for the $^5D_4 \rightarrow {}^7F_5$ transition in the Tb:$CePO_4$ samples prepared by conventional heating (CH) with different Tb content and in the $Tb_{0.02}Ce_{0.98}PO_4$ sample obtained by microwave heating (MW). Inset: evolution of the lifetimes with Tb content for the Tb:$CePO_4$ samples prepared by conventional heating.

Fig. 8. Excitation (λ_{em}= 542 nm) (top) and emission (λ_{ex}= 255 nm) (bottom) spectrum of the $Tb_{0.02}Ce_{0.98}PO_4$ sample obtained by microwave heating. The emission spectrum of the $Tb_{015}Ce_{0.85}PO_4$ sample synthesized by conventional heating is also included (bottom).

Fig. 9. Ce3d XPS spectra recorded for the $Tb_{0.15}Ce_{0.85}PO_4$ sample obtained by conventional heating and for $Tb_{0.02}Ce_{0.98}PO_4$ sample obtained by microwave heating

Fig. 10. Z potential for the $Tb_{0.02}Ce_{0.98}PO_4$ sample obtained by microwave heating as function of pH

Fig. 11. FTIR spectra recorded for the $Tb_{0.02}Ce_{0.98}PO_4$ sample obtained by microwave heating before and after functionalization with aspartic-dextran. The spectrum of the later is also included for comparison.

Fig. 12. TGA curves registered for the $Tb_{0.02}Ce_{0.98}PO_4$ sample obtained by microwave heating before and after functionalization with aspartic-dextran.

Fig. 13. Evolution of the UV-visible spectra recorded for the functionalized $Tb_{0.02}Ce_{0.98}PO_4$ nanophosphors dispersed in water (pH=6.7) with aging time.

Fig. 14. Cytotoxicity profiles of the $Tb_{0.02}Ce_{0.98}PO_4$ nanoparticles with VERO cells as determined by MTT assay. Percentage of viability of cells was expressed relative to control cells (n = 5). Results are represented as mean ± standard deviations.

Figure 1
Click here to download high resolution image

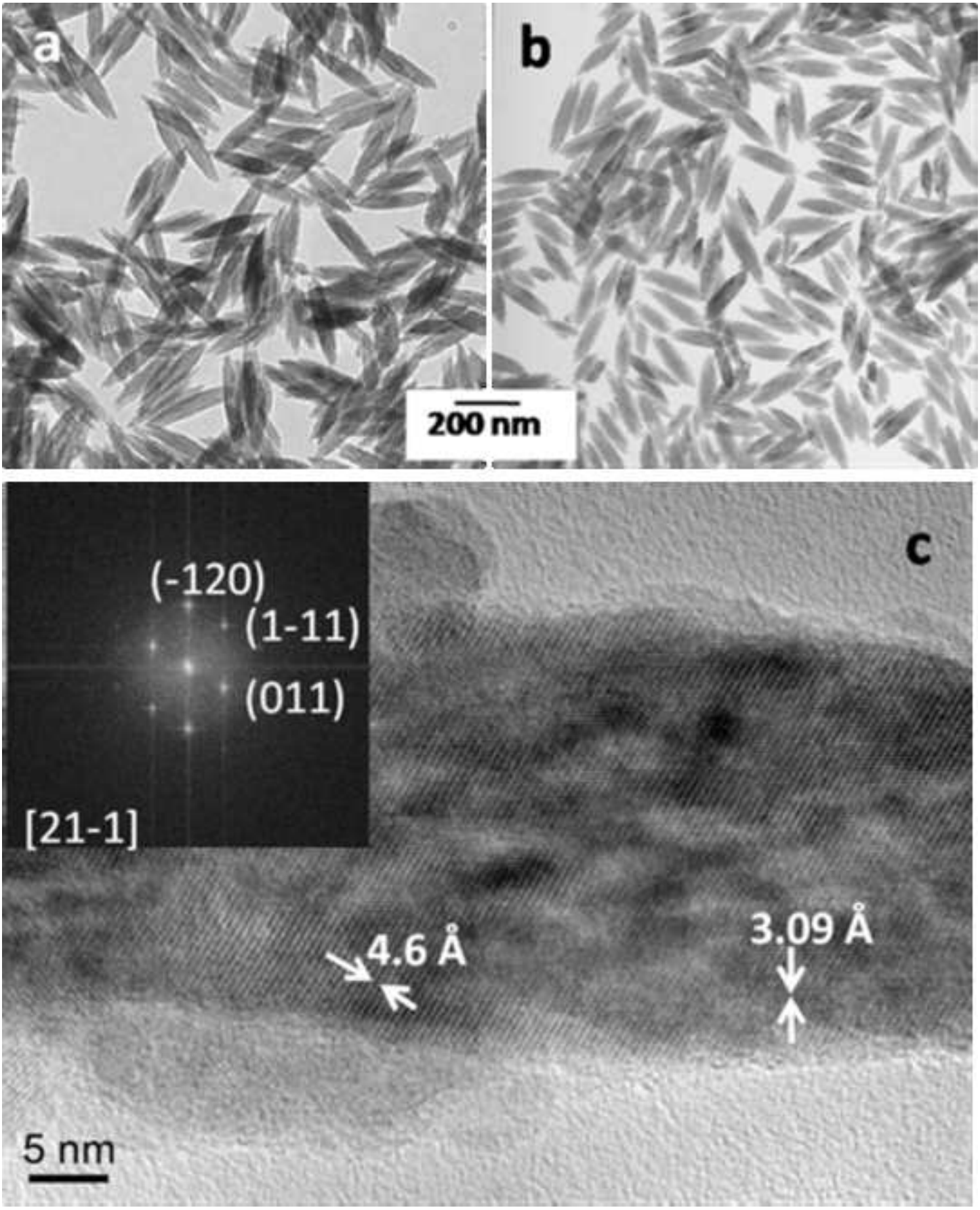

Figure 2
Click here to download high resolution image

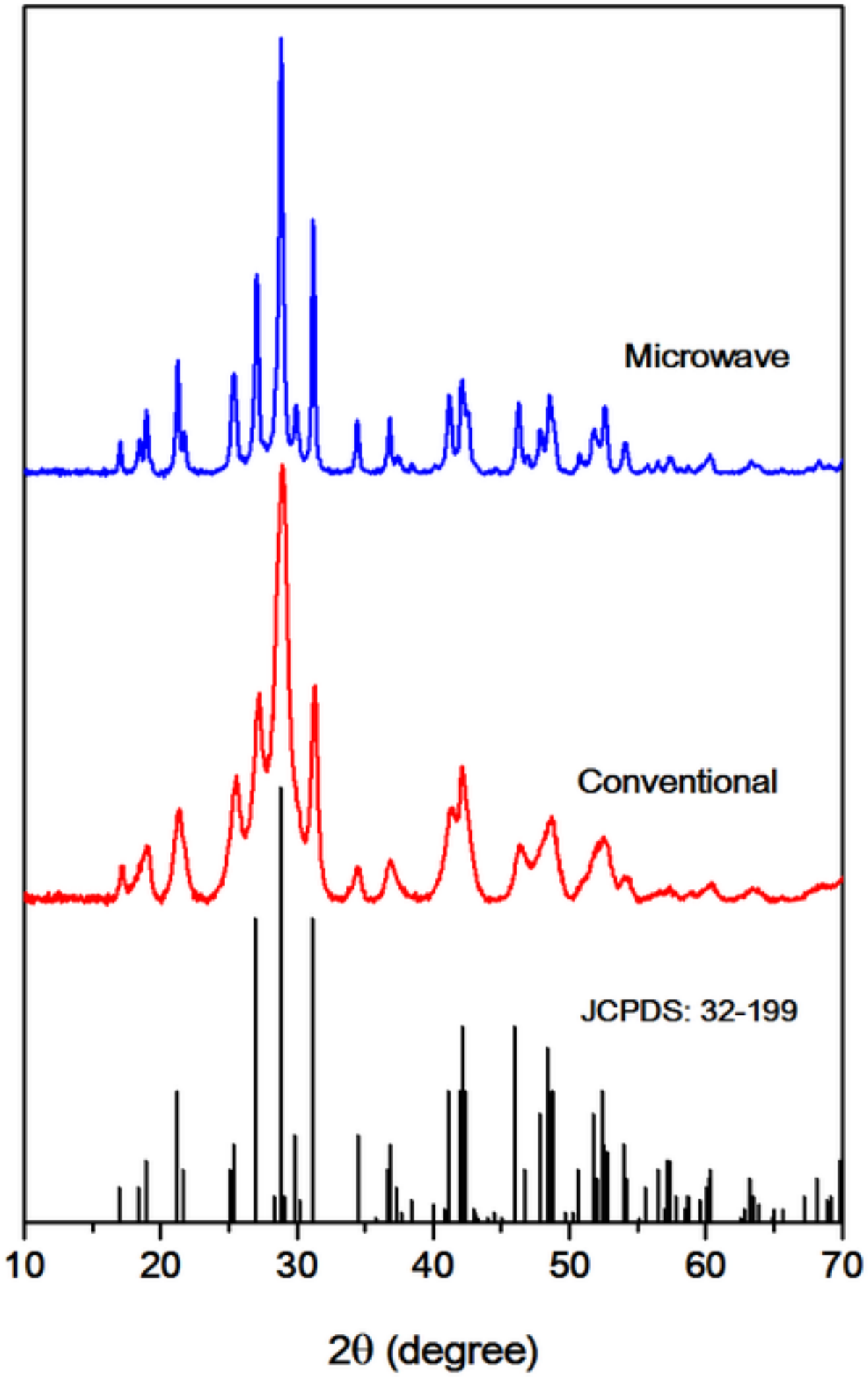

Figure 3
Click here to download high resolution image

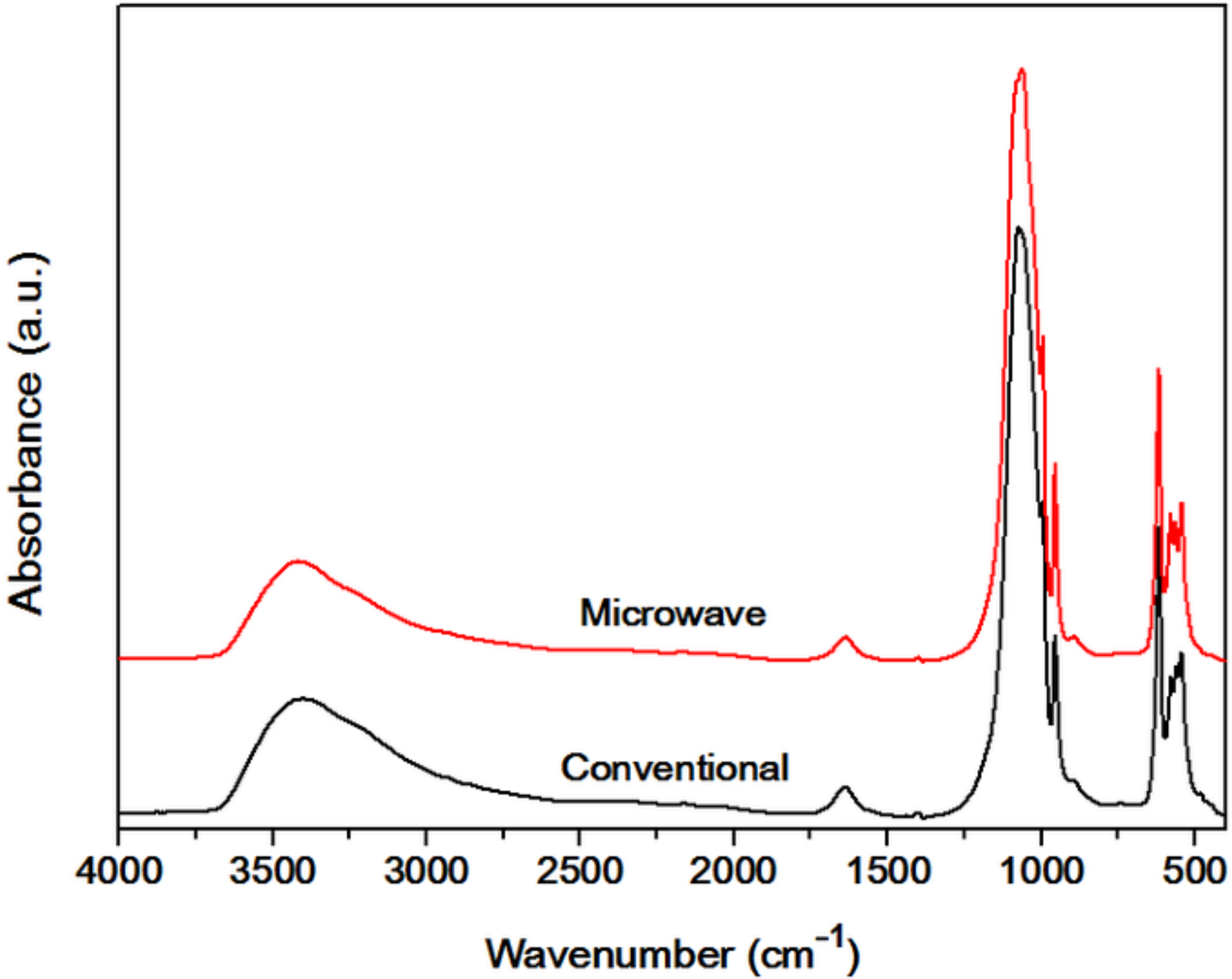

Figure 4
Click here to download high resolution image

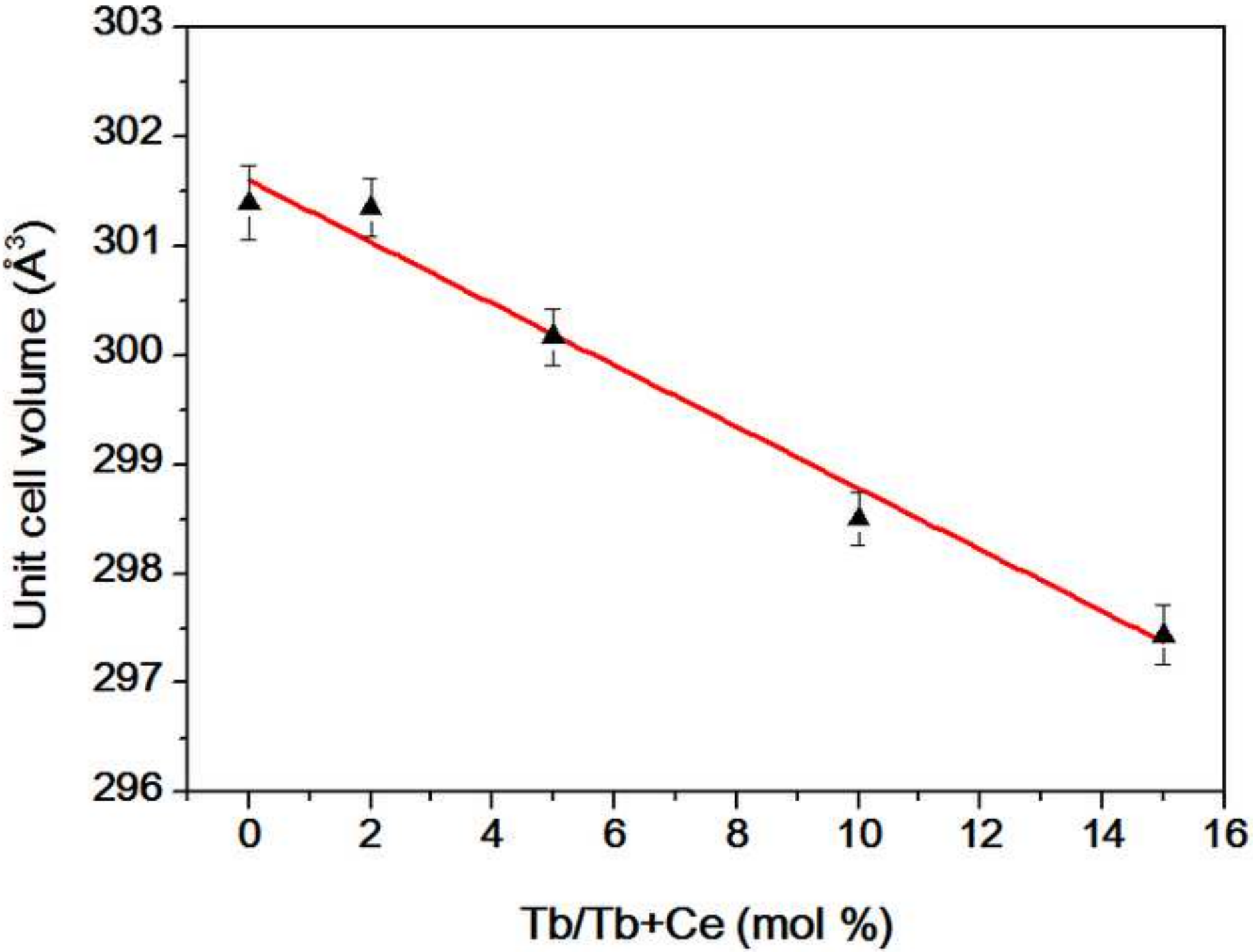

Figure 5
Click here to download high resolution image

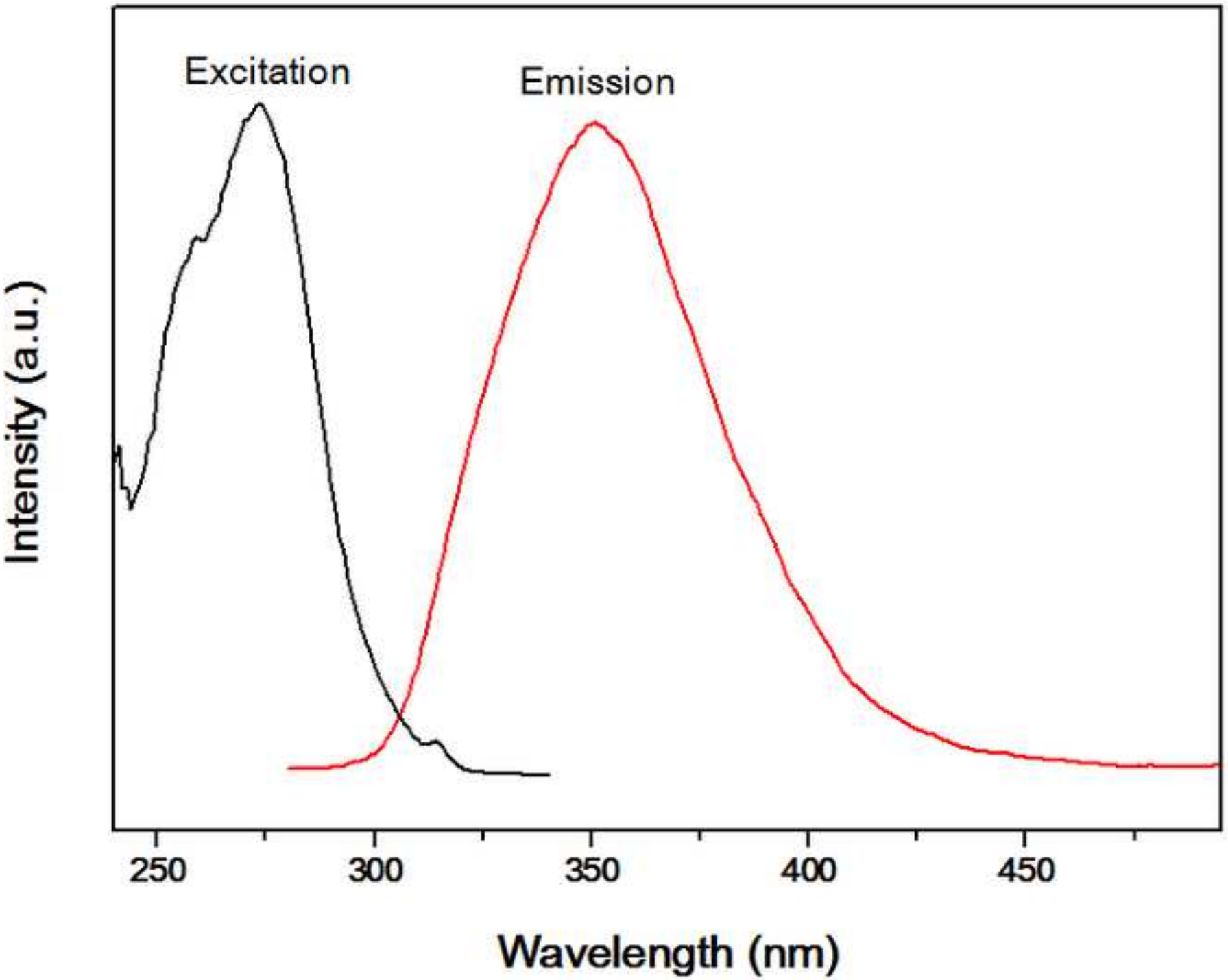

Figure 6
Click here to download high resolution image

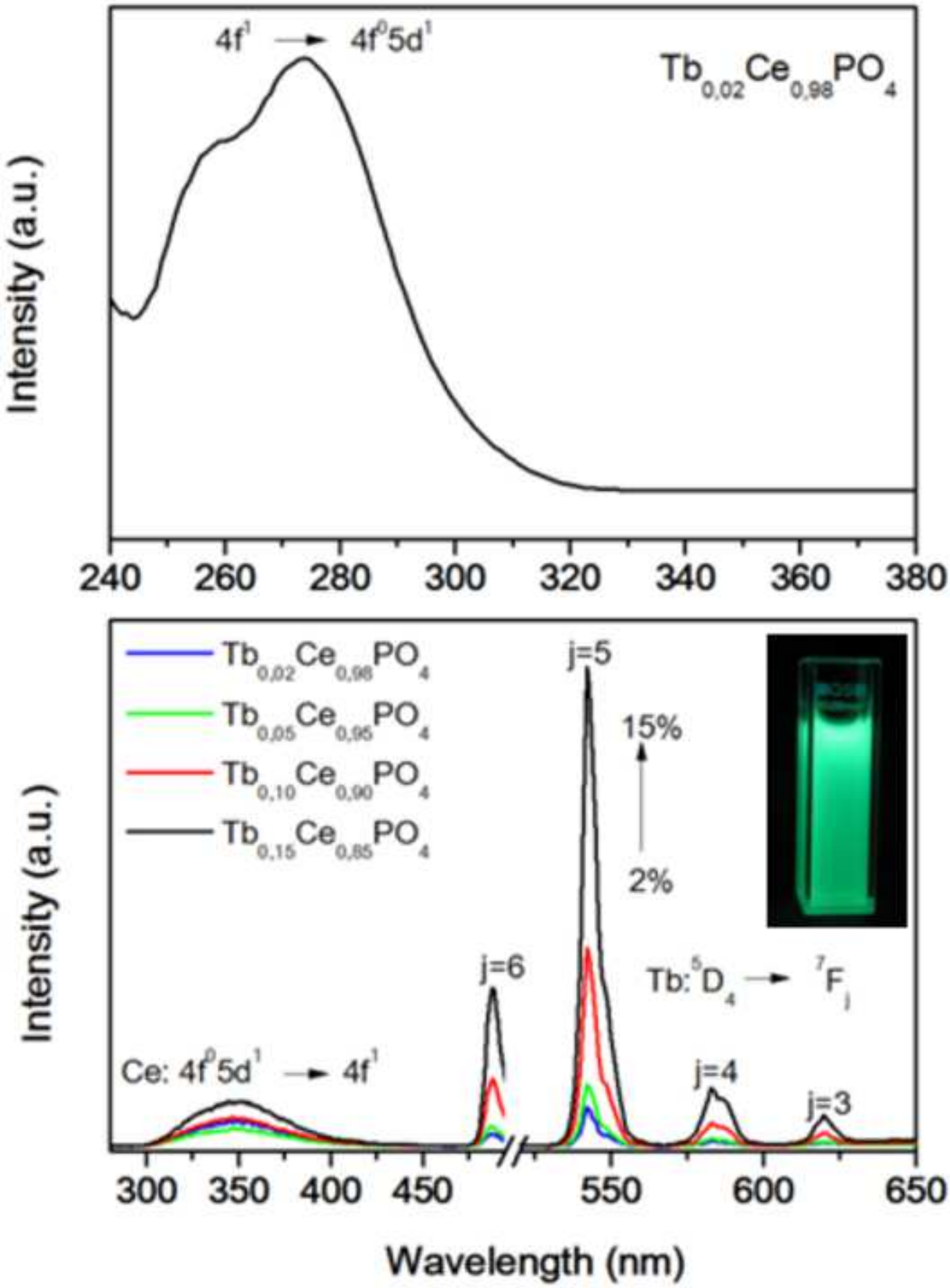

Figure 7
Click here to download high resolution image

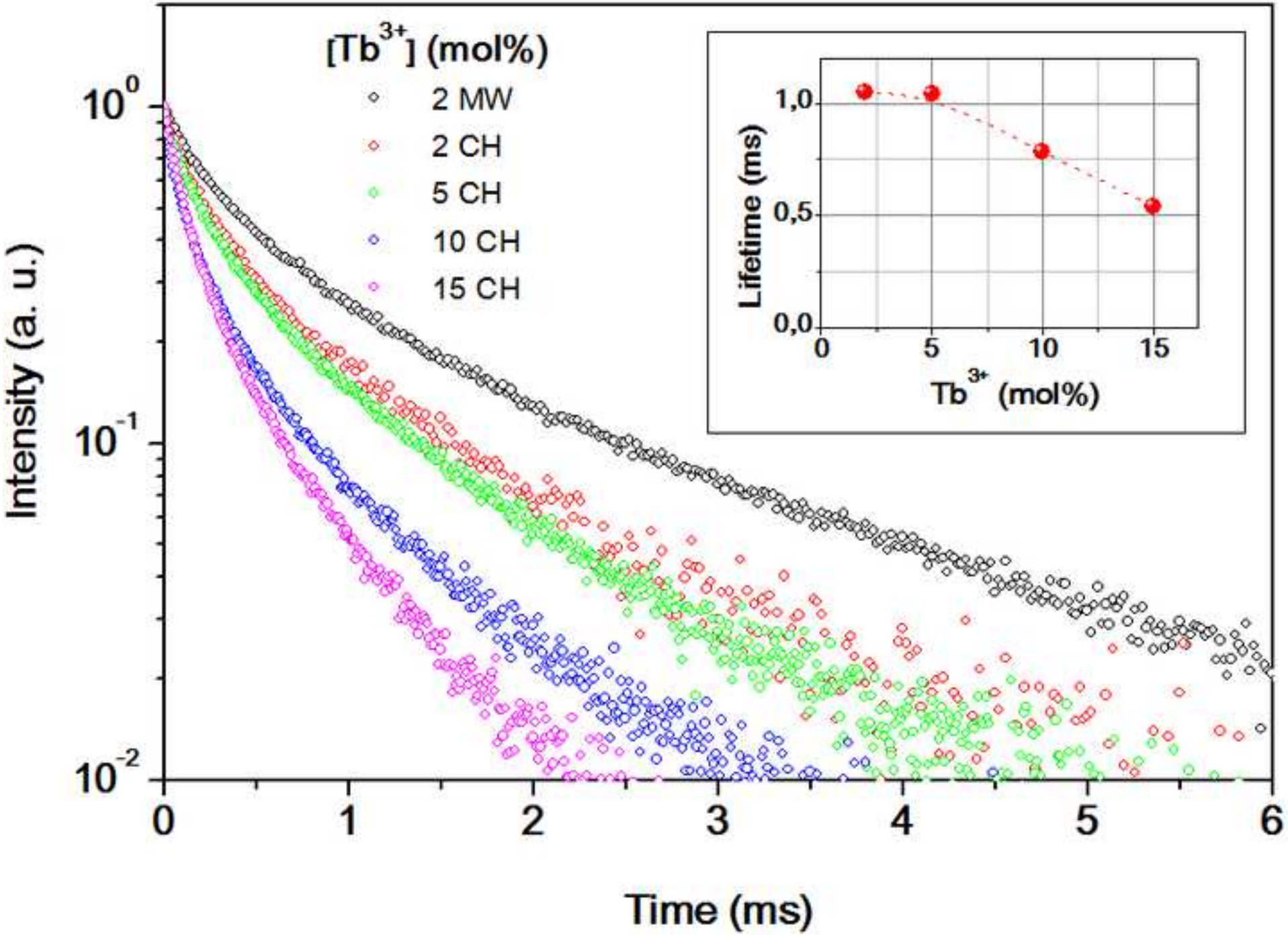

Figure 8
Click here to download high resolution image

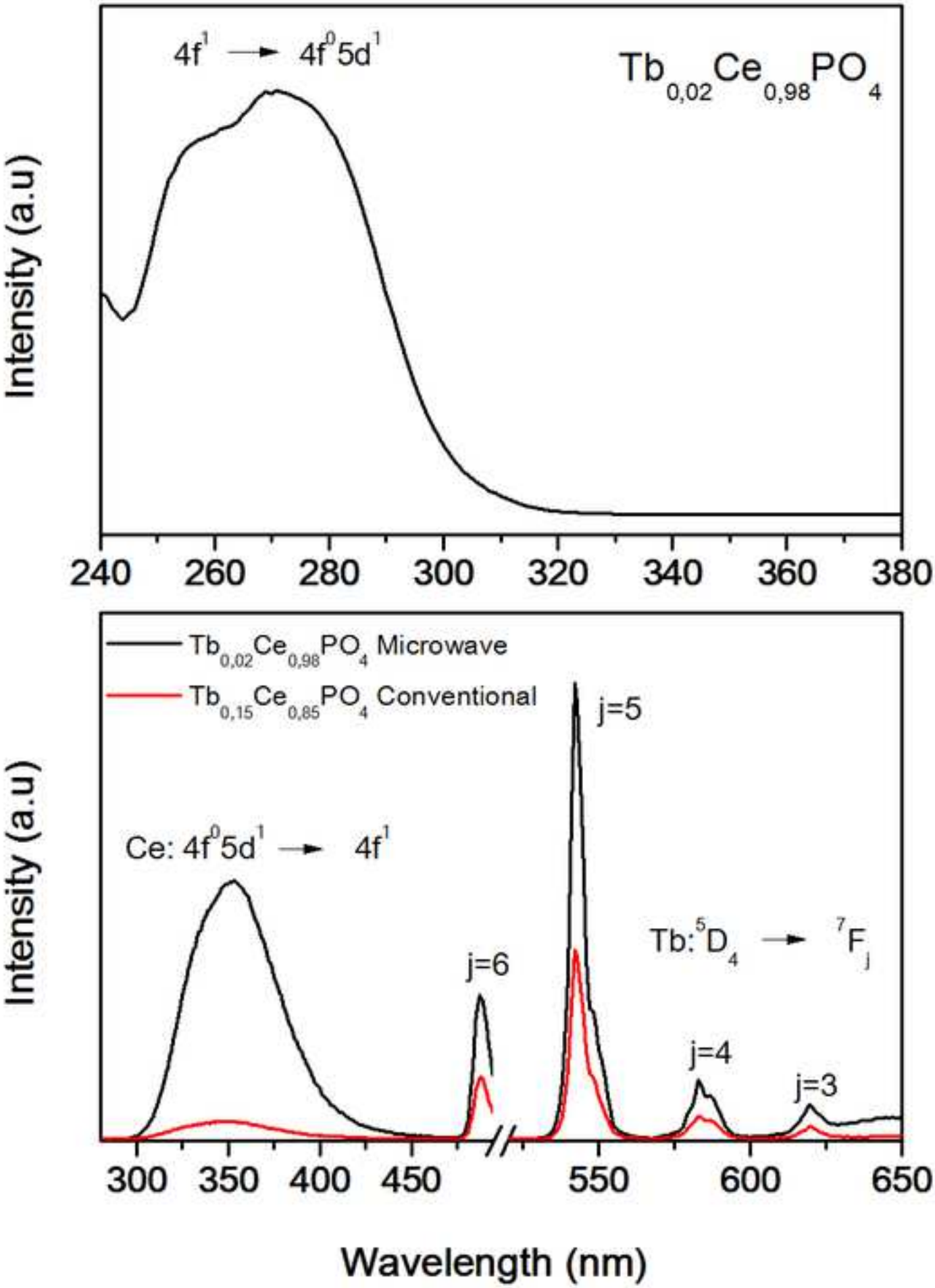

Figure 9
Click here to download high resolution image

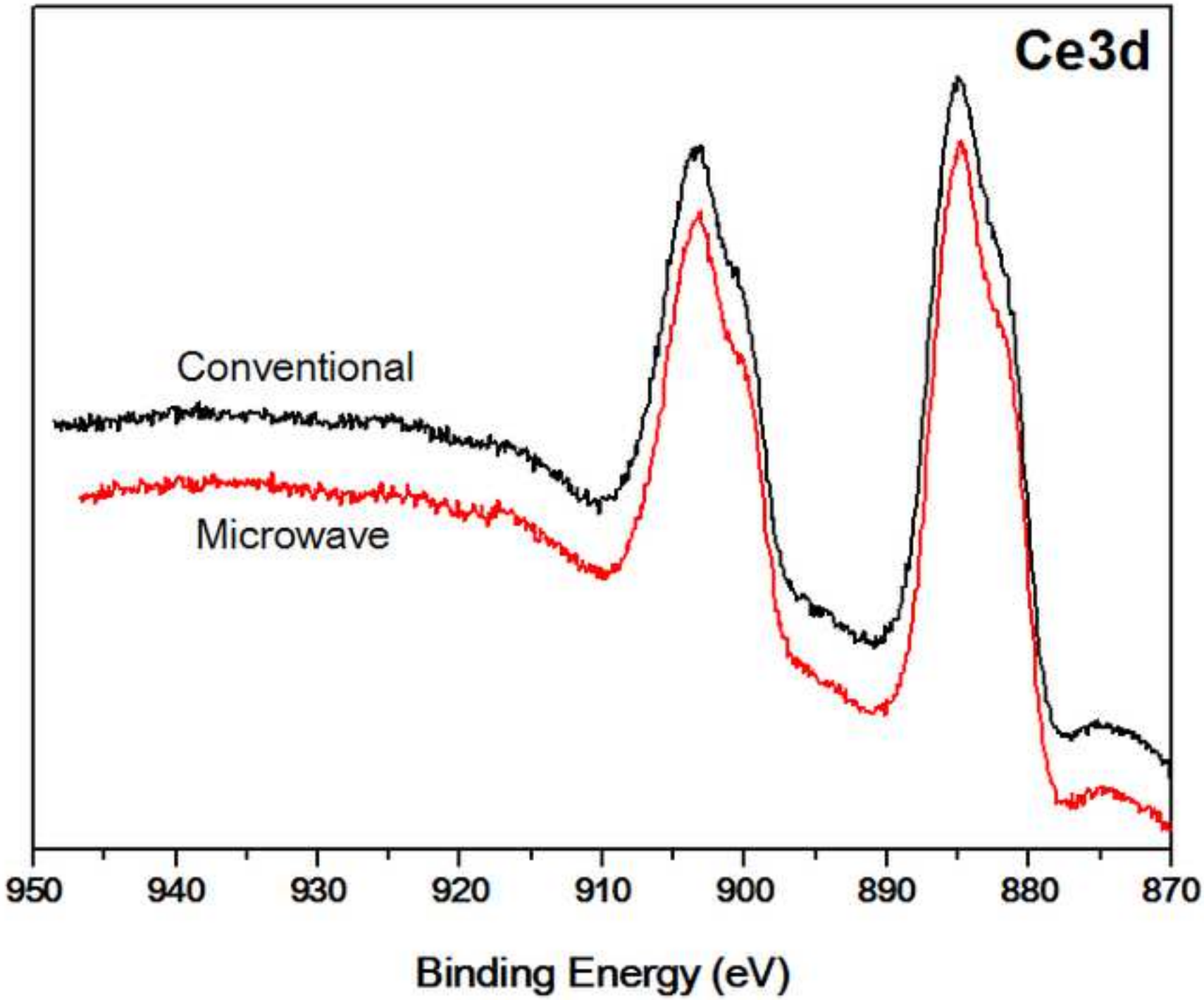

Figure 10
Click here to download high resolution image

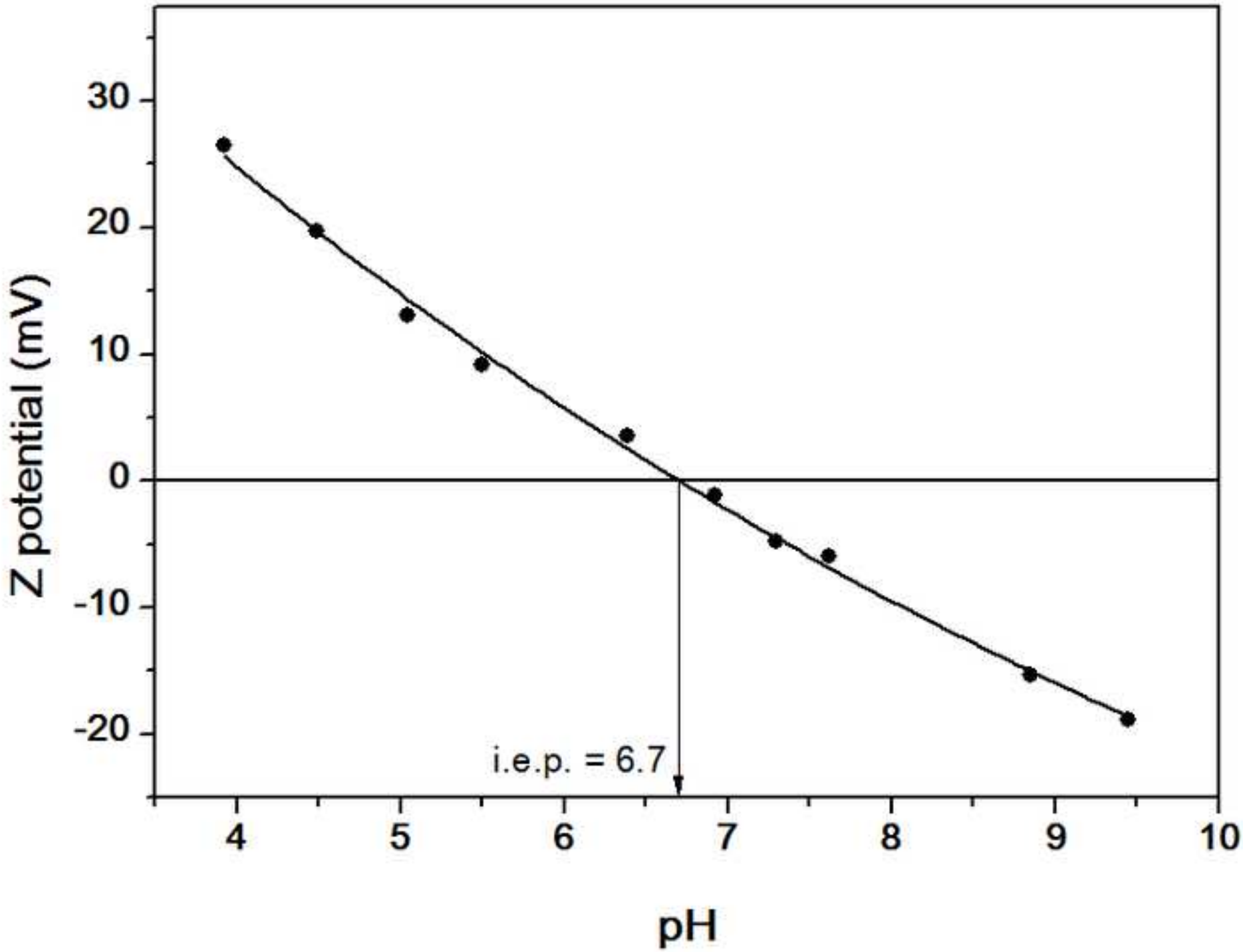

Figure 11
Click here to download high resolution image

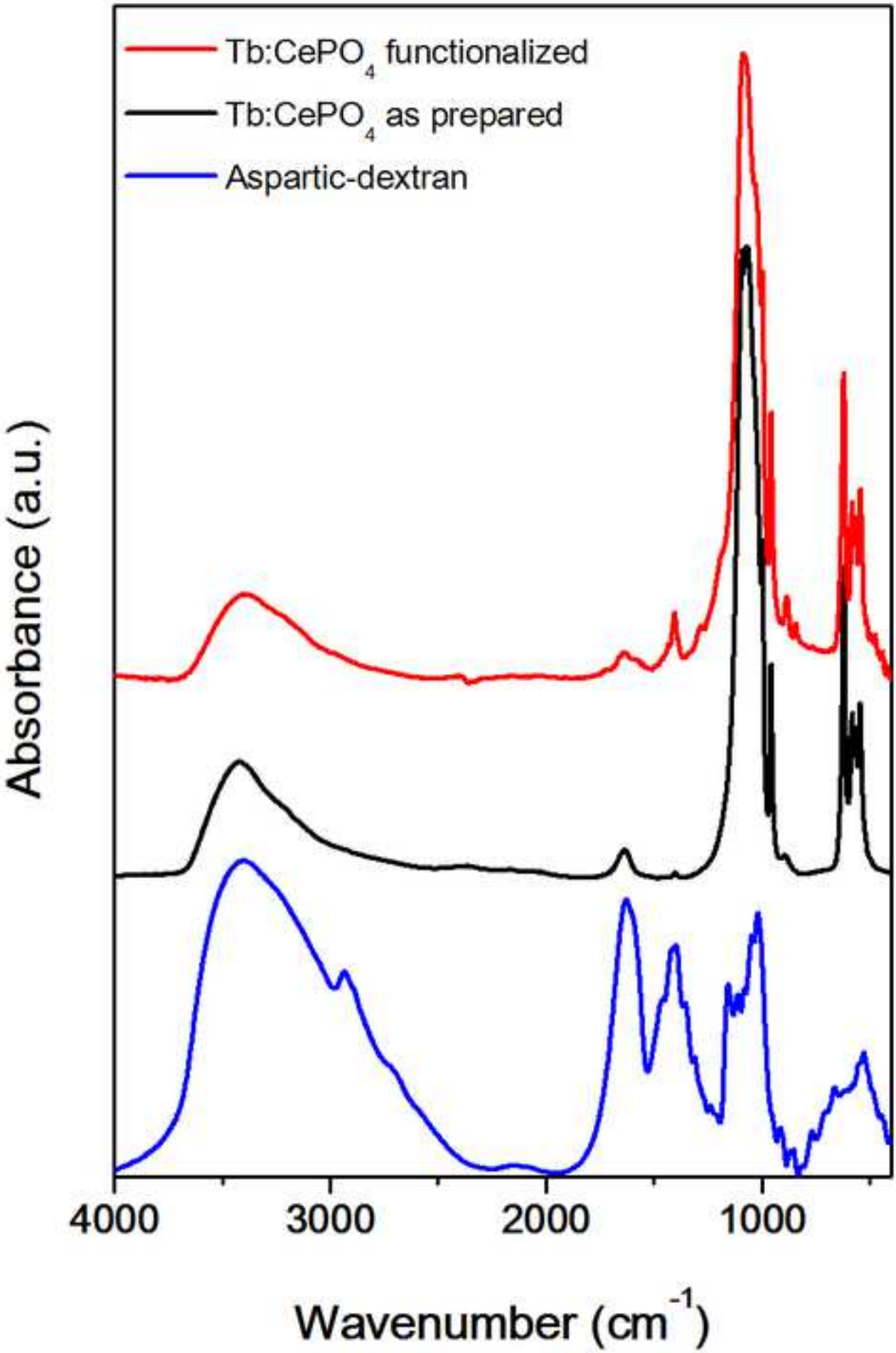

Figure 12
Click here to download high resolution image

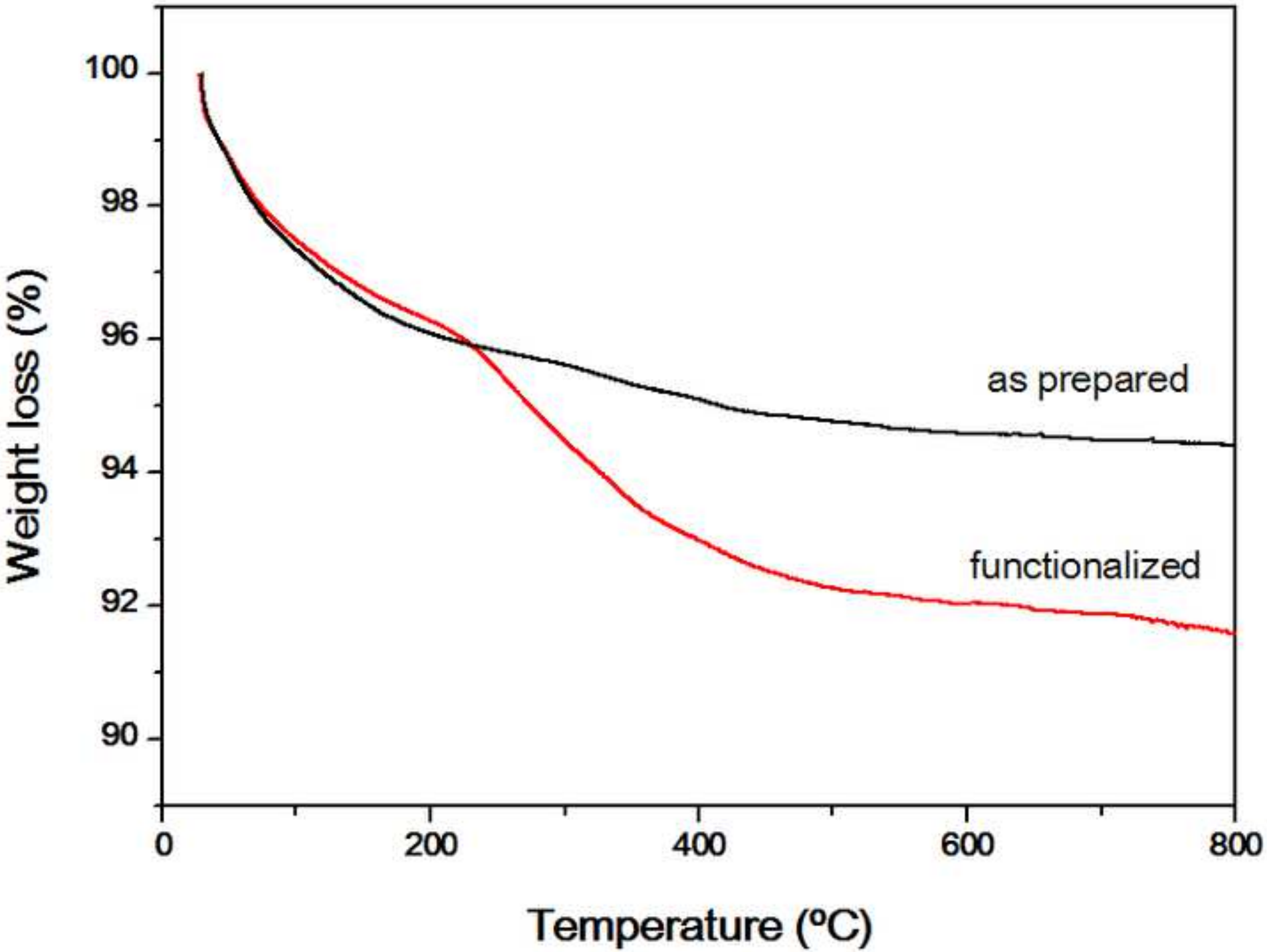

Figure 13
Click here to download high resolution image

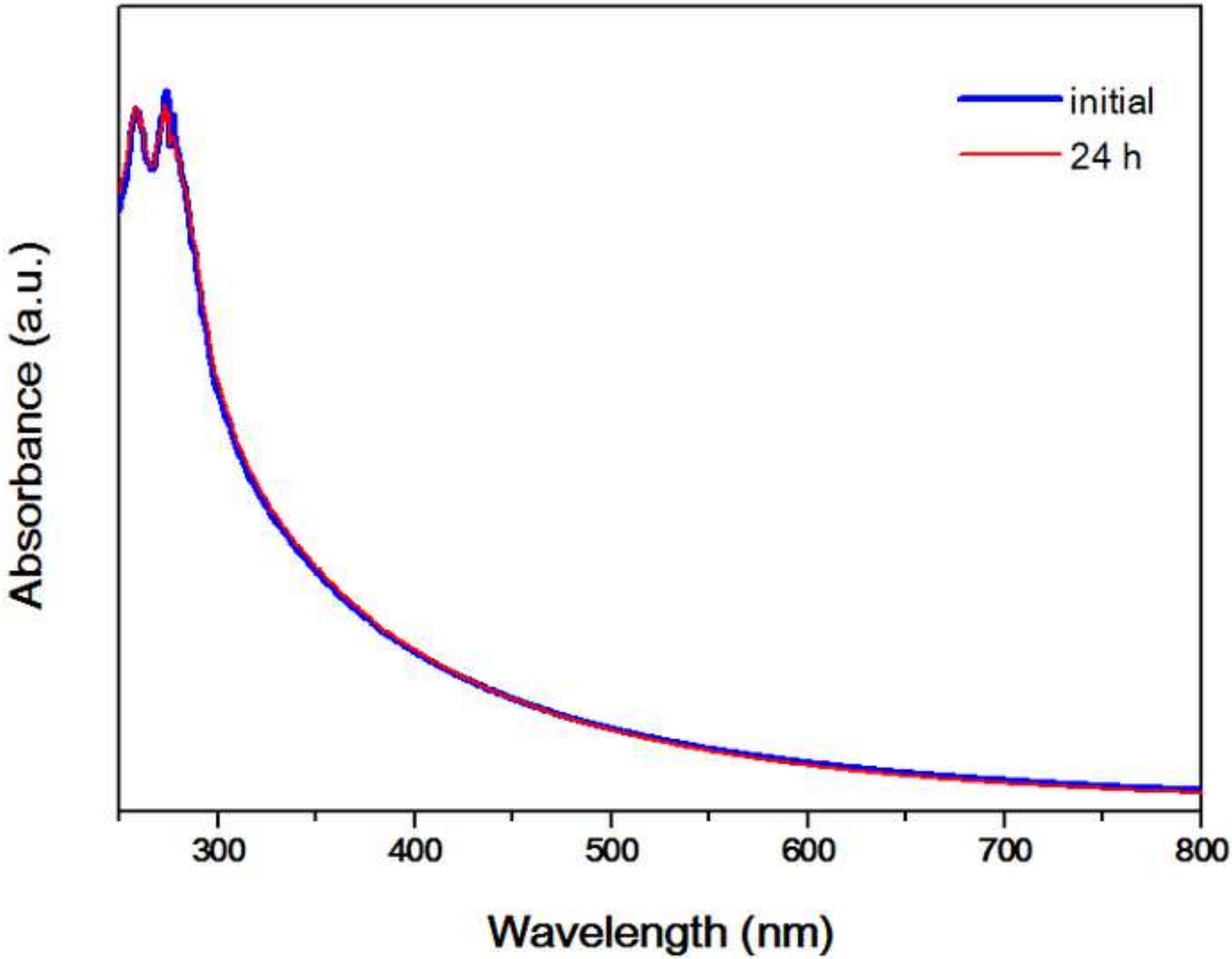

Figure 14
Click here to download high resolution image

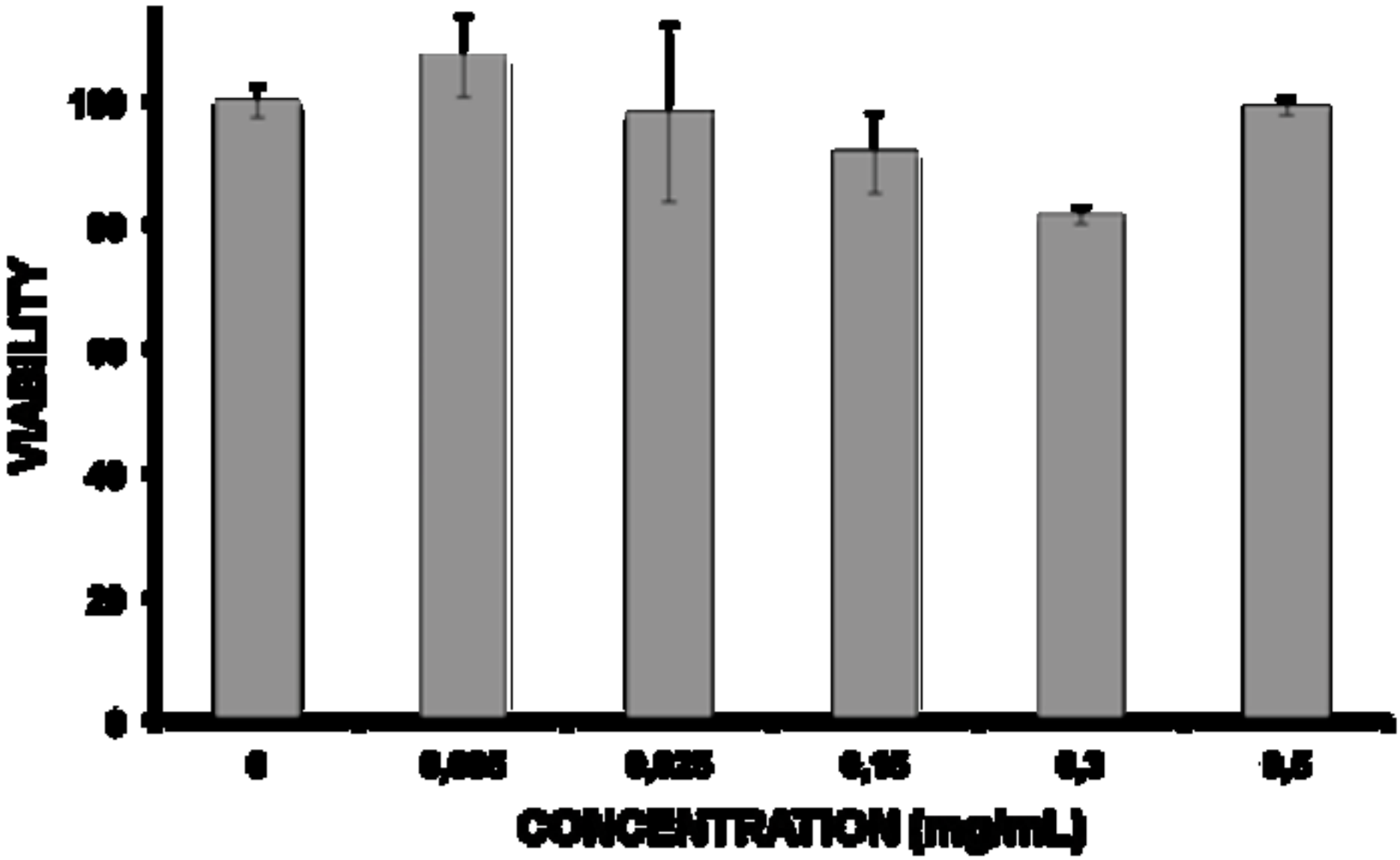

Supplementary material (audio/video files etc)

Click here to download Supplementary material (audio/video files etc): Suplementary Information.pdf

Supplementary Material

Synthesis and functionalization of biocompatible Tb:$CePO_4$ nanophosphors with spindle-like shape

Sonia Rodriguez-Liviano,[†] Francisco J. Aparicio,[†] Ana I. Becerro,[†] Jorge García-Sevillano,[‡] Eugenio Cantelar,[‡] Sara Rivera,[#] Yulán Hernández,[#] Jesus M de la Fuente, [#] Manuel Ocaña[†]*

[†]Instituto de Ciencia de Materiales de Sevilla (CSIC-US), Americo Vespucio 49, Isla de La Cartuja, 41092 Sevilla, Spain.

[#]Instituto de Nanociencia de Aragon, Universidad de Zaragoza, Mariano Esquillor s/n, Zaragoza, 50018, Zaragoza, Spain

[‡] Dpto. Física de Materiales, C-04. Universidad Autónoma de Madrid, 28049 Madrid, Spain.

*Corresponding Author: Manuel Ocaña. E-mail: mjurado@icmse.csic.es

Preparation and FTIR characterization of Aspartic-Dextran.

For the aspartic-dextran preparation, aldehyde-dextran was first obtained by oxidation of 1.67 g of dextran (Dextran from Leuconostoc mesenteroides, $(C_6H_{10}O_5)_n$ average mol wt 15,000-30,000, Sigma-Aldrich) dissolved in water (50 cm^{-3}) with 0.8 g of sodium periodate ($INaO_4$,≥99.0%, Sigma-Aldrich). The oxidation was performed overnight at room temperature under magnetic stirring. Once the reaction was finished, the solution was dialyzed against double distilled water for 24 h using a dialysis tubing cellulose membrane. The dextran obtained under these conditions has 20% of the glucose molecules present in the polymer oxidized as di-aldehydes.

The aldehyde-dextran so obtained was mixed first with an equal volume of a 3 M aspartic acid (L-Aspartic acid, $C_4H_7NO_4$, ≥98% Sigma -Aldrich) solution at pH 7.5 (adjusted with NaOH), and then with solid trimethylaminoborane (Borane Trimethylamine Complex, TMAB, $C_3H_{12}BN$, ≥95,0% Fluka) which was dissolved until its final concentration reached 150 mM. By so doing, the amino groups of the aspartic acid reacted with the aldehyde groups in the dextran. After 15 h, the obtained aspartic-dextran was reduced to stabilize the Schiff's bases formed and any remaining aldehyde. For this purpose, 10 mg cm^{-3} of sodium borohydride ($NaBH_4$, ≥98,5% Sigma-Aldrich) were first added to the above solution after which, the pH was adjusted at 10 by adding NaOH. Then, sodium borohydride was added again in a similar proportion (10 mg cm^{-3}). This mixture was kept under magnetic stirring for 2 h at room temperature after which, the pH of the mixture was lowered to 6 using hydrochloric acid to destroy the sodium borohydride excess. Once the dextran was modified with aspartic acid and reduced, it was dialyzed, first, against a sodium acetate 10 mM solution at pH 4 and then against double distilled water (twice).

In addition to the bands due to dextran, the FTIR spectrum of the solid obtained after drying an aliquot of the aspartic-dextran solution deposited on silicon wafer (Fig. S1) clearly showed two strong absorption in the 1600-1400 cm^{-1} region, which must be ascribed to the aspartate groups (López-Navarrete JT, Hernández V, Ramírez FJ (1994) Biopolymers 1065-1077), thus confirming the success of our synthesis procedure.

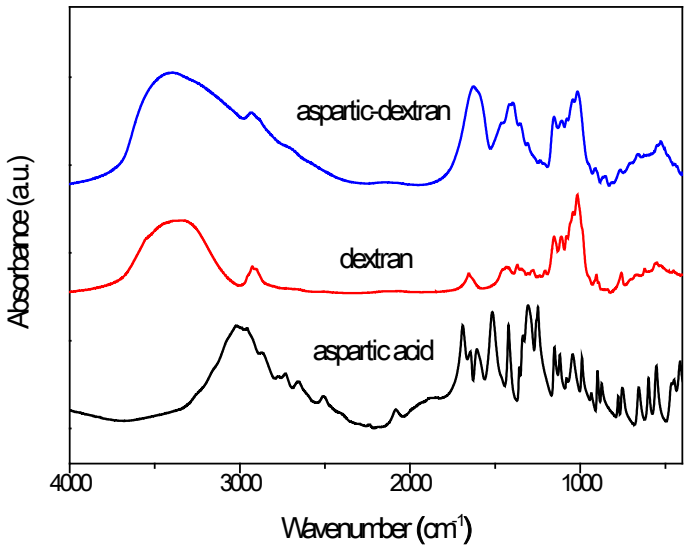

Fig. S1. FTIR spectra of dextran, aspartic acid and aspartic-dextran.

Characterization of $CePO_4$ based nanoparticles

Table S1: Crystal size (nm) determined from different XRD reflections for the Tb doped $CePO_4$ samples synthesized by conventional heating with different Tb content (% Tb/Ce+Tb mol ratio).

		Crystal size (nm)				
2θ	**hkl**	**0%Tb**	**2%Tb**	**5%Tb**	**10%Tb**	**15%Tb**
≈27	200	10	35	48	74	116
≈31.2	-122	20	30	48	82	82
≈34.5	-202	17	41	41	110	83

Table S2: Nominal and experimental (ICP) Tb/Ln (Ln=Tb+Ce) mol ratio for the Tb doped $CePO_4$ samples synthesized by conventional and microwave heating.

Sample	Heating mode	Tb/Ln (nominal) Mol ratio (%)	Tb/Ln (ICP) Mol ratio (%)
$Tb_{0.02}Ce_{0.98}PO_4$	Conventional	2	2,20
$Tb_{0.05}Ce_{0.95}PO_4$	Conventional	5	4,88
$Tb_{0.10}Ce_{0.90}PO_4$	Conventional	10	10.11
$Tb_{0.15}Ce_{0.85}PO_4$	Conventional	15	16,42
$Tb_{0.02}Ce_{0.98}PO_4$	Microwave	2	1,82

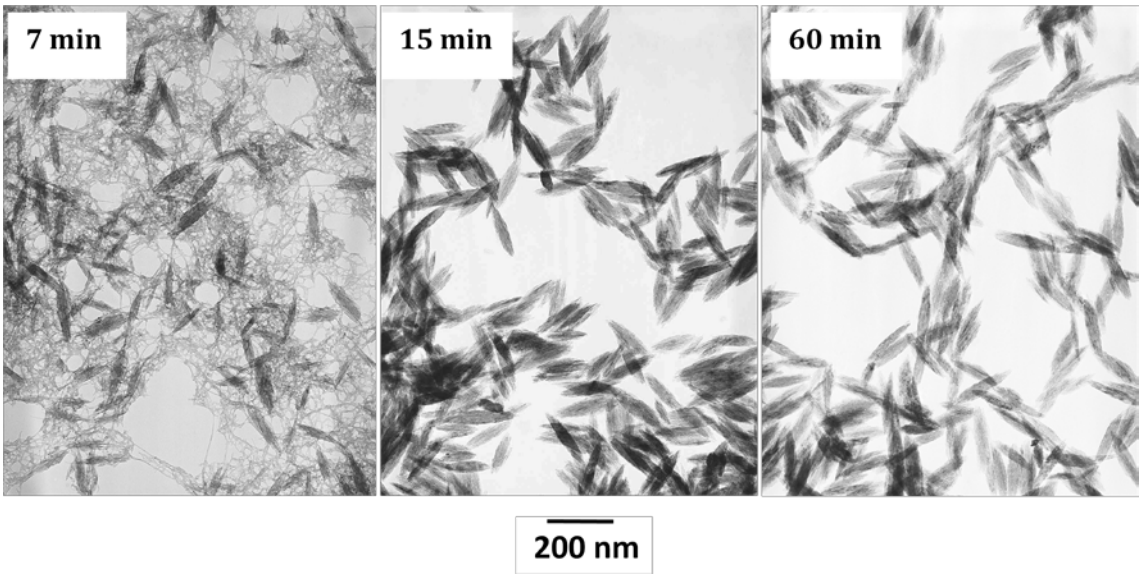

Fig. S2. TEM images of the $CePO_4$ nanoparticles prepared by aging 0.004 $Ce(acac)_3$ mol dm^{-3} and 0.15 mol dm^{-3} H_3PO_4 EG solutions at 120ºC for different periods of time, using a conventional oven.

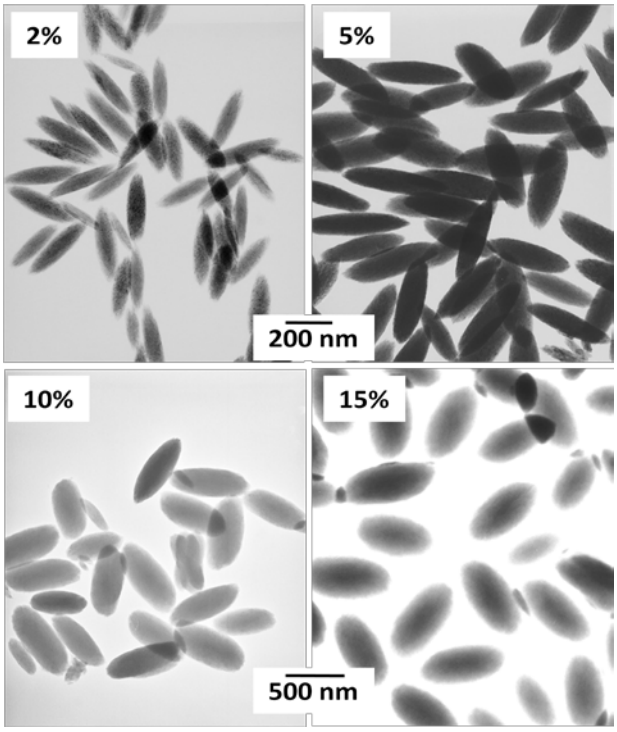

Fig. S3. TEM images of the Tb doped $CePO_4$ nanoparticles prepared with different Tb content (% Tb/Ce+Tb mol ratio) by conventional heating.

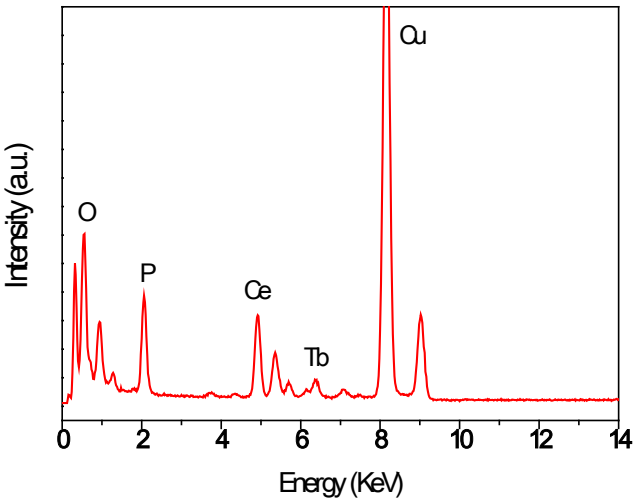

Fig. S4. EDX spectrum obtained for the $Tb_{0.15}Ce_{0.85}PO_4$ sample prepared by conventional heating

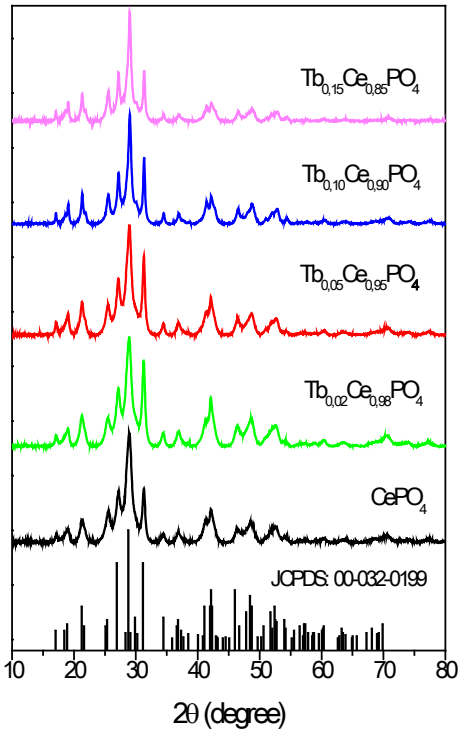

Fig. S5. X-ray diffraction patterns recorded for the Tb doped $CePO_4$ nanoparticles prepared by conventional heating. The JCPDS file for monoclinic $CePO_4$ is also included.

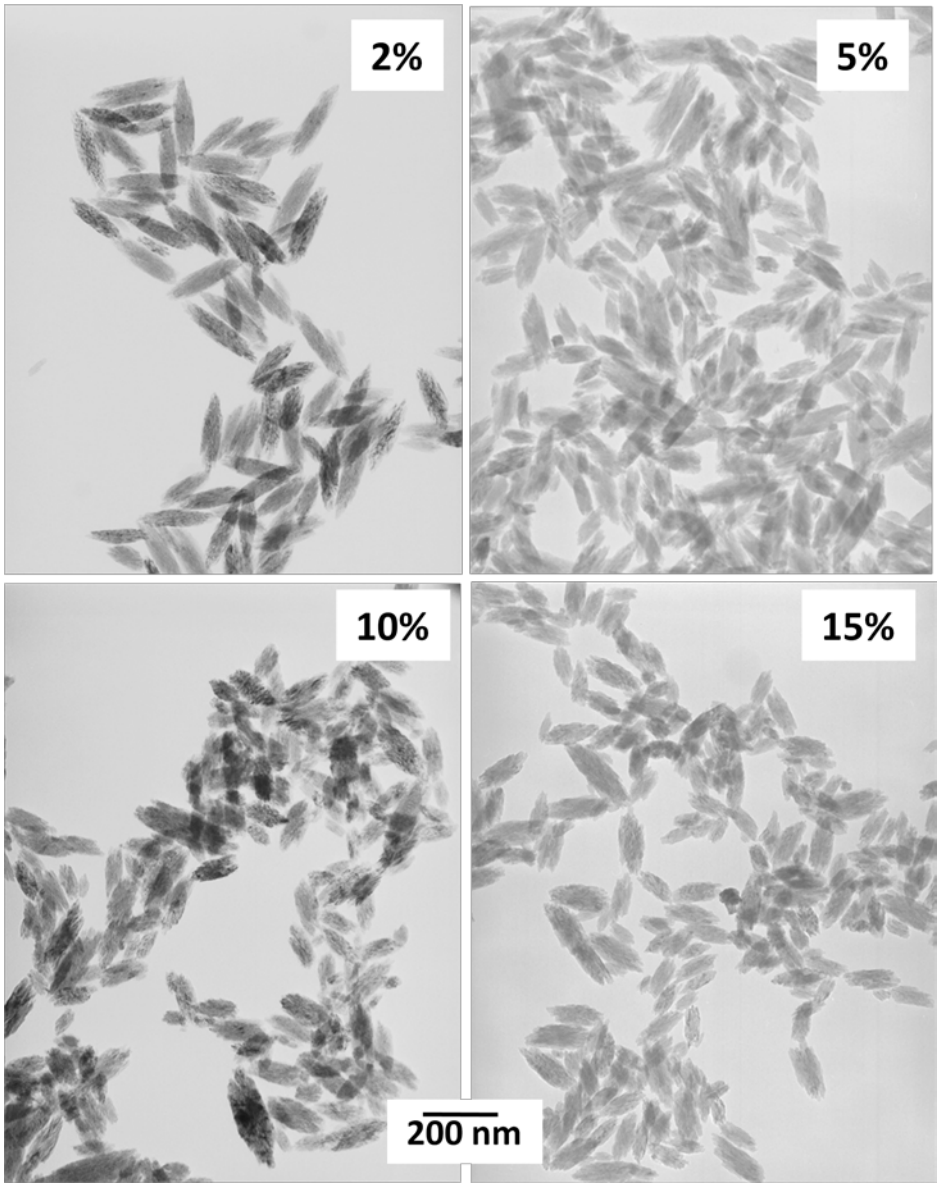

Fig. S6. TEM images of the Tb doped $CePO_4$ nanoparticles prepared with different Tb content (% Tb/Ce+Tb mol ratio) by microwave-assisted heating.

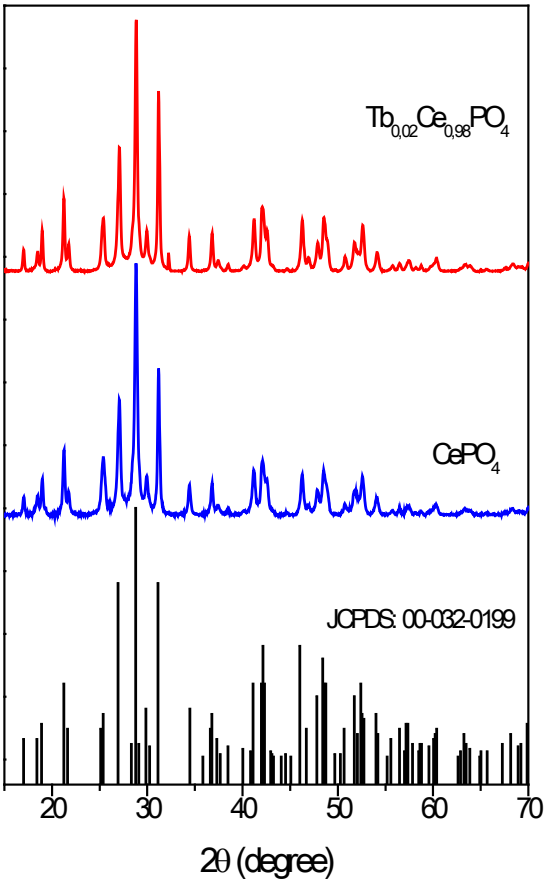

Fig. S7. X-ray diffraction patterns recorded for the $CePO_4$ and $Tb_{0.02}Ce_{0.98}PO_4$ nanoparticles prepared by microwave heating. The JCPDS file for monoclinic $CePO_4$ is also included.

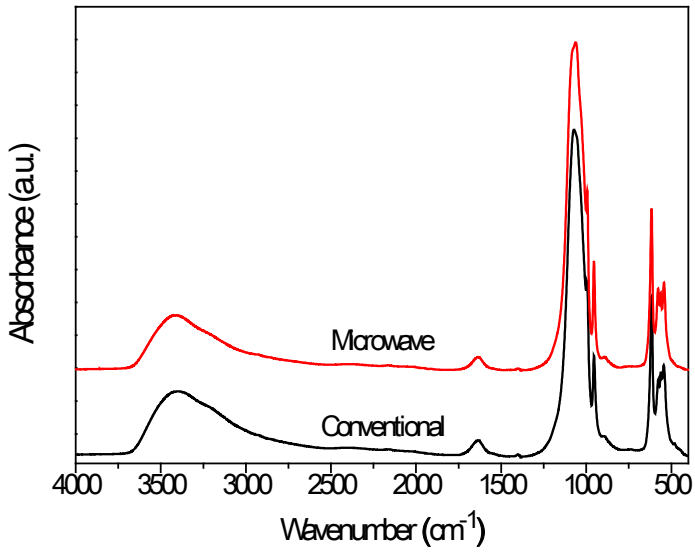

Fig. S8. FTIR spectra recorded for the $Tb_{0.02}Ce_{0.98}PO_4$ sample obtained by microwave heating and for the $Tb_{015}Ce_{0.85}PO_4$ sample synthesized by conventional heating.

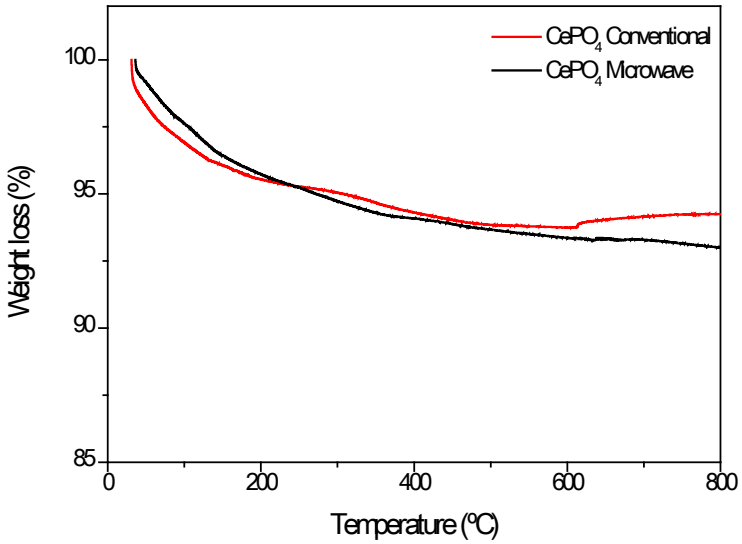

Fig. S9. TGA curves obtained for the $Tb_{0.15}Ce_{0.85}PO_4$ sample obtained by conventional heating and for $Tb_{0.02}Ce_{0.98}PO_4$ sample obtained by microwave heating

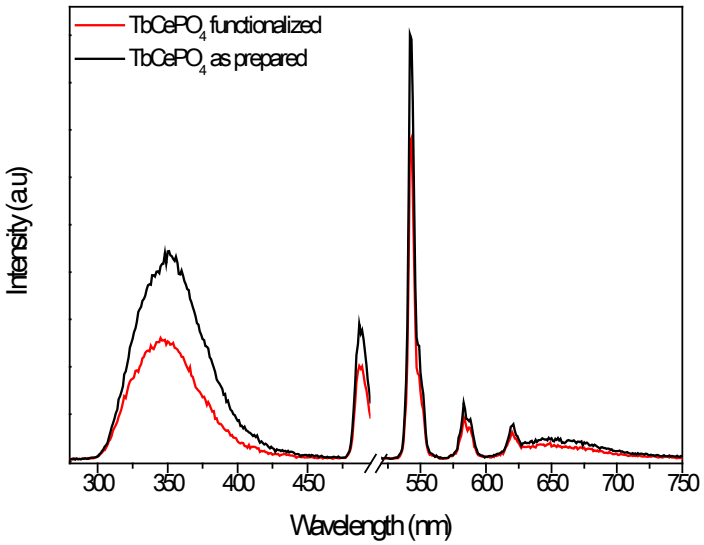

Fig. S10. Emission spectrum (λ_{ex}= 255 nm) recorder for the $Tb_{0.02}Ce_{0.98}PO_4$ sample obtained by microwave heating before and after functionalization with aspartic-dextran.